metals

Article

On the Solidification and Phase Stability of Re-Bearing High-Entropy Superalloys with Hierarchical Microstructures

Wei-Che Hsu [1,2], Takuma Saito [3], Mainak Saha [3], Hideyuki Murakami [4], Taisuke Sasaki [3] and An-Chou Yeh [1,2,*]

[1] Department of Materials Science and Engineering, National Tsing Hua University, 101, Section 2, Kuang-Fu Road, Hsinchu 300044, Taiwan; s104031593@m104.nthu.edu.tw
[2] High Entropy Materials Center, National Tsing Hua University, 101, Section 2, Kuang-Fu Road, Hsinchu 300044, Taiwan
[3] Microstructure Analysis Group, Materials Evaluation Field, Research Center for Structural Materials, National Institute for Materials Science (NIMS), 1-2-1 Sengen, Tsukuba 305-0047, Japan; takuma.saito@ruhr-uni-bochum.de (T.S.); saha.mainak@nims.go.jp (M.S.); sasaki.taisuke@nims.go.jp (T.S.)
[4] Research Center for Structural Materials, National Institute for Materials Science, 1-2-1 Sengen, Tsukuba 305-0047, Japan; murakami.hideyuki@nims.go.jp
* Correspondence: yehac@mx.nthu.edu.tw

Abstract

This study presents the design and microstructural investigation of a single-crystal (SX) Re-bearing high-entropy superalloy (HESA-X1) featuring a thermally stable γ–γ'–γ hierarchical microstructure. The alloy exhibits FCC γ nanoparticles embedded within $L1_2$-ordered γ' precipitates, themselves distributed in a γ matrix, with the suppression of detrimental topologically close-packed (TCP) phases. To elucidate solidification behavior and phase stability, Scheil–Gulliver and TC-PRISMA simulations were conducted alongside SEM and XRD analyses. Near-atomic scale analysis in 3D using Atom Probe Tomography (APT) revealed pronounced elemental partitioning, with Re strongly segregating to the γ matrix, while Al and Ti were preferentially enriched in the γ' phase. Notably, Re demonstrated a unique partitioning behavior compared to conventional superalloys, facilitating the formation and stabilization of γ nanoparticles during two-step aging (Ag-2). These γ nanoparticles significantly contribute to improved mechanical properties. Long-term aging (up to 200 h) at 750–850 °C confirmed exceptional phase stability, with minimal coarsening of γ' and retention of γ nanoparticles. The coarsening rate constant K of γ' at 750 °C was significantly lower than that of Re-free HESA, confirming the diffusion-suppressing effect of Re. These findings highlight critical roles of Re in enhancing microstructural stability by reducing atomic mobility, enabling the development of next-generation HESAs with superior thermal and mechanical properties for high-temperature applications.

Keywords: Re-bearing HESA; solidification; elemental partitioning; hierarchical microstructure; phase stability

Academic Editor: Jose Manuel Torralba

Received: 20 June 2025
Revised: 10 July 2025
Accepted: 19 July 2025
Published: 22 July 2025

Citation: Hsu, W.-C.; Saito, T.; Saha, M.; Murakami, H.; Sasaki, T.; Yeh, A.-C. On the Solidification and Phase Stability of Re-Bearing High-Entropy Superalloys with Hierarchical Microstructures. *Metals* **2025**, *15*, 820. https://doi.org/10.3390/met15080820

1. Introduction

High-entropy materials (HEMs) have emerged as a novel class of materials characterized by high configurational entropy, offering unique structural and functional properties [1–5]. Among these, high-entropy alloys (HEAs) have attracted significant attention as promising alloy systems for structural applications. The basic definition of HEA, which contains at least five or more major elements and each of which does not exceed 35 at.%,

was first proposed by Yeh [1]. HEAs have been reported to exhibit excellent mechanical and chemical properties, such as high hardness [6,7], high wear resistance [8,9], and good corrosion resistance [10,11]. For high-temperature applications, precipitation and solid solution strengthening are considered. It had been reported that the tensile strength of HEAs could be enhanced by precipitation strengthening [12–14] or nitride HEA [15]. In addition, refractory HEAs are important for high-temperature applications and have been the focus of significant research and development [16–18]. However, the elevated temperature tensile strength of HEA could be limited by insufficient fractions and relatively low solvus of strengthening phases in HEAs [19]. Additionally, refractory high-entropy alloys tend to display inferior tensile properties at high temperatures compared to conventional superalloys [20]. Therefore, according to previous studies [21–23], nickel-based superalloys exhibit superior mechanical properties at high temperatures around 600 °C to 1050 °C and have been widely used so far as turbine engines or blades in aerospace and energy industries. Their superior high-temperature mechanical properties have resulted from the coherent $L1_2$-ordered γ' precipitates embedded in the face-centered cubic (FCC) γ matrix. Therefore, the high-entropy superalloy (HESA), which combines the advantages of nickel-based superalloys and HEA, was proposed [24]. From a thermodynamic perspective, HESAs possess inherent advantages over conventional superalloys, as their elevated configurational entropy increases the solubility limits within the γ matrix. This broader solubility range helps stabilize the matrix against the formation of detrimental phases and enhances compositional flexibility compared to conventional superalloys [25,26]. In addition, the precipitation strengthening with γ' precipitates and solid solution strengthening of γ matrix allow HESAs to possess higher hardness and tensile strength than those of conventional HEAs throughout the temperatures [27,28]. However, the strength of the HESAs is still lower than that of commercial superalloys such as CMSX-4 and CMSX-10 at high temperatures. Recently, the development of HESAs has provided new pathways for creating advanced materials with exceptionally high-temperature performance via the design of heat treatments. The heat treatment remains a crucial aspect of materials engineering, directly controlling microstructural characteristics and thus determining the mechanical properties of metallic alloys. Optimizing heat treatment processes enables precise manipulation of hierarchical microstructures in HESAs, significantly improving their performance under high-temperature conditions.

Typically, the microstructure of $L1_2$-strengthened HESAs originates from a single-phase solid solution formed during high-temperature solution treatment and subsequently evolves into a dual-phase γ/γ' structure upon aging. Under optimized heat treatment conditions, further microstructural evolution can occur, resulting in the formation of nanoscale, disordered γ particles embedded within ordered $L1_2$ γ' precipitates, thus generating a unique γ–γ'–γ hierarchical microstructure. Chen et al. [29] have demonstrated the improved mechanical properties of HESAs at high temperatures with the presence of γ-γ'-γ hierarchical microstructure, which consists of FCC γ nanoparticles forming inside $L1_2$-ordered γ' precipitates embedded in the FCC γ matrix. The high-temperature yielding and ultimate tensile strength of γ-γ'-γ strengthened HESAs are much higher than those of the alloys in the same chemical composition without hierarchical γ-γ'-γ precipitations. However, the underlying mechanism and the driving force of the γ particle formation remain unclear. Moreover, the stability of the hierarchical microstructure would also be an issue because the γ-γ'-γ microstructure is in a metastable state and may disappear through the re-dissolving of γ nanoparticles into the matrix at elevated temperature. Strategies for solving these problems will be critical to further applications.

Apart from the heat treatment histories, partitioning of elements between the γ phase and γ' precipitate plays a crucial role in determining the mechanical properties, such as

strength, creep resistance, and thermal stability in conventional superalloys [30,31]. Elemental partitioning significantly influences the lattice misfit between γ and γ′ phases, a critical factor governing γ′ morphology and coarsening behavior under stress [22]. HESAs reported to date typically exhibit a positive lattice misfit; for example, HESA-3 demonstrates a misfit value of +0.08% at 982 °C [29]. Alloys with positive lattice misfits have demonstrated superior resistance to cyclic creep compared to alloys with negative misfits [32,33], as cyclic creep conditions closely mimic the operational environment of turbine engines. Consequently, systematic investigation of the cyclic creep behavior of HESAs is recommended for future studies to thoroughly evaluate their potential in high-temperature structural applications.

In the present work, SX Re-bearing HESA with adequate addition of refractory elements, hereafter designated as HESA-X1, was developed. The addition of refractory elements to HESA has been shown to reduce the diffusion rate of elements, thereby inhibiting phase transformations [22]. However, the underlying mechanisms driving this phenomenon remain unclear. Consequently, understanding the partitioning behavior, as well as the thermodynamics and kinetics of each phase, is crucial when incorporating refractory elements. The current research, therefore, integrates experimental analyses with advanced simulation methods to investigate the solidification profile, precipitation kinetics of γ′ precipitates, and γ nanoparticles. Scheil–Gulliver simulations, implemented using Thermo-Calc software (version 2025a, Thermo-Calc Software AB, Stockholm, Sweden) with Calculation of Phase Diagram (CALPHAD)-based calculations, were utilized to accurately predict the non-equilibrium solidification behavior and elemental partitioning between solid and liquid phases in the HESA-X1 alloy. Additionally, the precipitation kinetics of γ and γ′ phases were simulated using the TC-Prisma module based on Langer–Schwartz theory [34] and Kampmann–Wagner numerical modeling [35]. This combined experimental and computational approach provided comprehensive insights into the prediction of the hierarchical γ–γ′–γ microstructure, including the ability to estimate the characteristic dimensions of each phase. It also demonstrated the role of γ nanoparticles in enhancing creep resistance and elucidated the underlying mechanisms responsible for their formation in the Re-bearing HESA-X1 alloy.

2. Materials and Method

2.1. Materials and Processing

The chemical composition of the Re-bearing high-entropy superalloy, designated HESA-X1, is presented in Table 1. The SX HESA-X1 samples were directionally solidified along the [001] crystallographic orientation using the Bridgman method, conducted by the Superalloys and High-Temperature Materials Group at the National Institute for Materials Science (NIMS), Japan.

Table 1. Composition of Re-bearing HESA-X1 based on constant at.%.

	Ni	Co	Fe	Cr	Al	Ti	Mo	W	Re	Ta	Hf
HESA-X1	50.87	20	3	6	12	5	0.5	1	1	0.6	0.03

The as-cast SX HESA-X1 alloy sample was homogenized at 1275 °C for 8 h, then followed by air cooling to room temperature. After solution treatment, the HESA-X1 was treated with two different aging treatments, Ag-1 and Ag-2. The Ag-1 was a one-step aging treatment at 1100 °C for 2 h, followed by air cooling, while Ag-2 meant a two-step aging treatment at 1100 °C for 2 h with air cooling and then aging at 750 °C for 20 h, followed by water quenching. The time–temperature profiles of these two heat treatment procedures are illustrated in Figure 1.

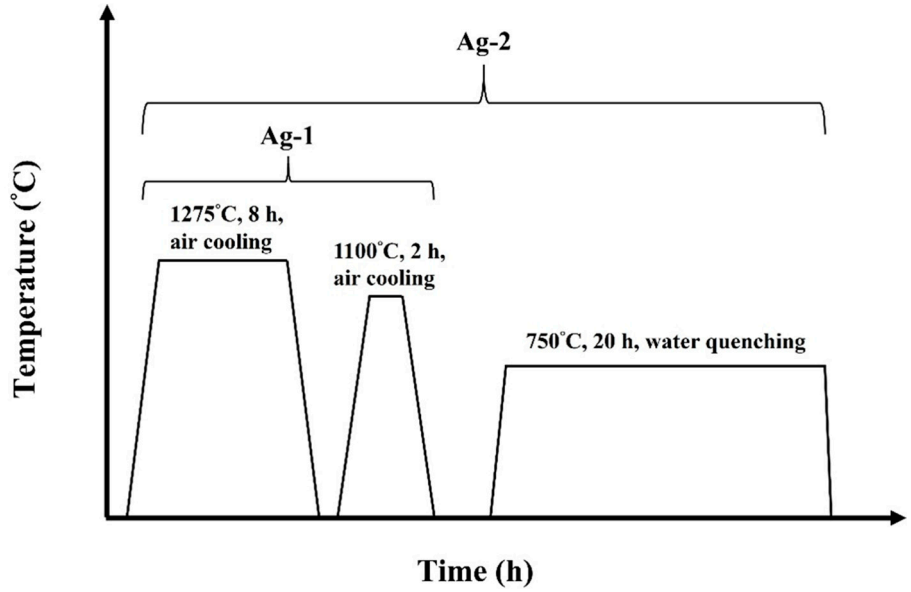

Figure 1. Schematic illustration of the heat treatment processes for Ag-1 and Ag-2.

2.2. Microstructural Observations and Calculations

Microstructural evaluation of the HESA-X1 alloy was carried out using Scanning Electron Microscopy (SEM: JSM-7200, JEOL, Tokyo, Japan) and Transmission Electron Microscopy (TEM: JEM-F200, JEOL, Tokyo, Japan) following standard metallographic preparation procedures involving grinding and twinjet polishing in a solution containing 10% $HClO_4$ + 90% C_2H_5OH at 30 V and −25 °C. Quantitative assessments of γ' precipitate size and volume fraction, as well as the presence of FCC γ nanoparticles, were performed using Image J analysis software (version 1.53a, National Institutes of Health, Bethesda, Maryland, USA). X-ray diffraction (XRD) analyses of the HESA-X1 alloys were conducted on a Shimadzu XRD-6000 instrument (Shimadzu Corp., Kyoto, Japan) with Cu Kα radiation, operating at 30 kV and 20 mA, over a 2θ range of 20° to 100° at room temperature.

The equilibrium phase diagram of the HESA-X1 alloy was constructed using Thermo-Calc simulation and with the TCHEA7 database. The non-equilibrium solidification pathway was subsequently evaluated using the Scheil–Gulliver model implemented within the same framework. Precipitation kinetics of γ' and γ phases were analyzed using the TC-Prisma module with the thermodynamic database TCHEA7 and the kinetics database MOBHEA2. Local Electron Atom Probe (LEAP 5000XS, CAMECA Inc., Madison, WI, USA) was used for Atom Probe Tomography (APT) analysis. APT specimens were prepared by a focused ion beam (FIB) (Helios 650, Thermo Fisher Scientific, Waltham, MA, USA) system with the standard lift-out procedure along [100] direction for HESA-X1 alloys. APT data were collected in laser mode with laser wavelength: 355 nm, laser pulse rate: 250 kHz, energy: 25 pJ, detection rate: 1%, and specimen temperature: 50 K. The APT mass spectrum was acquired based on the principles of field evaporation and time-of-flight mass spectrometry. Under a high electric field, surface atoms are ionized and evaporated as positively charged ions, which are then accelerated toward a position-sensitive detector. The time-of-flight of each ion is recorded and used to determine its mass-to-charge ratio (m/z), allowing reconstruction of a mass spectrum with identifiable elemental and isotopic peaks by using CAMECA IVAS 3.8.2 software. For example, Re is detected at ~185 and 187 Dalton for Re^{+}, and ~92.5 and 93.5 Dalton for Re^{2+}. In addition, measurements of the size and volume fraction of FCC γ particles were taken based on the method highlighted in [36] and compared with SEM analysis results.

To investigate the thermal stability and coarsening behavior of γ′ precipitates, additional aging treatments were conducted on the HESA-X1 samples post Ag-1 treatment. These isothermal exposures were performed at temperatures ranging from 450 °C to 850 °C for varying durations (50, 100, and 200 h). Microstructural changes were examined using SEM (JSM-7200, JEOL, Tokyo, Japan). Furthermore, the extra two-step aging treatments following Ag-2 were conducted at 750 °C, 800 °C, and 850 °C for durations of 20, 100, and 200 h, respectively, to assess the stability of FCC γ nanoparticles.

2.3. Mechanical Tests

Vickers hardness measurements were performed on the HESA-X1 alloy after the Ag-1 heat treatment using a Future-Tech FV-800 tester (Future-Tech Corp., Kawasaki, Japan). The horizontal cross-sections of the samples were tested under a 49 N load with a 15 s dwell time, and the average was determined from five indentations. Creep specimens were prepared from single-crystal bars fabricated via the Bridgman casting process. The bars were machined into specimens with a gauge section measuring 19 mm in length, 3.2 mm in width, and 2.4 mm in thickness. To achieve a uniform and defect-free surface finish, all specimen surfaces for both hardness and creep tests were mechanically ground with 2000-grit silicon carbide (SiC) abrasive paper. Creep tests were conducted at 760 °C under an applied tensile stress of 600 MPa, utilizing an ATS Series 2330 Lever Arm Creep Testing System (APPLIED TEST SYSTEMS, Butler, PA, USA). Three specimens were tested for both the Ag-1 and Ag-2 conditions to determine average values.

3. Results and Discussion

3.1. Solidification Process

HESAs are inherently complex multi-component systems in which solidification behavior is primarily governed by the partitioning of constituent elements between the solid and liquid phases. This partitioning critically influences the final microstructure and, in turn, the mechanical performance of these alloys under high-temperature conditions [37]. Due to differences in elemental solubility and melting points, significant chemical segregation often develops during solidification. The elements such as Cr, W, and Re, which possess much higher melting points, tend to concentrate within the dendritic cores. In contrast, lower melting point elements such as Ni, Ti, and Al become enriched in the interdendritic regions [38]. This non-uniform elemental distribution leads to compositional heterogeneities and promotes the formation of detrimental secondary phases, including Cr- and W-rich Laves phases and low-melting eutectic phases, both of which can degrade mechanical properties.

The solidification of HESAs involves a complex interplay between dendritic growth, elemental partitioning, and secondary phase formation. While experimental observations offer direct insight into microstructural evolution, computational thermodynamics is essential for predicting and understanding segregation behavior. The Scheil–Gulliver model, implemented in Thermo-Calc software (version 2025a, Thermo-Calc Software AB, Stockholm, Sweden), is a well-established approach for simulating non-equilibrium solidification and can provide accurate predictions of solute distribution during solidification. These simulations are essential for developing effective post-solidification heat treatment strategies that aim to homogenize the alloy and minimize segregation-induced defects [39–41].

In the present study, the HESA-X1 alloy was systematically investigated to elucidate the partitioning behavior of both refractory (Re, Mo, W, Ta, and Hf) and non-refractory (Ni, Co, Cr, Fe, Al, and Ti) elements between the solid and liquid phases. This elemental partitioning critically influences phase stability, segregation phenomena, and the subsequent formation of precipitates by the Scheil simulation. It was employed to predict compositional

gradients, offering valuable insights into how specific alloying elements govern microstructural evolution. Figure 2 presents the simulation results for the HESA-X1 alloy, illustrating pronounced chemical segregation and the resulting compositional heterogeneities across the solidification temperature range. As shown in Figure 2a, solidification begins and progresses with the sequential formation of various phases. Initially, a simple γ' phase appears, but as the solid fraction increases, secondary phases such as B2, μ phase, and σ phase emerge at lower temperatures, indicating a high tendency for the formation of the segregation-induced phase. Figure 2b,c presented the compositional evolution of solute elements in the remaining liquid as a function of solid fraction. In Figure 2b, Ni remains the dominant element in the liquid, while Ti and Al show increasing concentrations as solidification proceeds, suggesting strong partitioning into the interdendritic liquid. Similarly, Mo and Ta exhibit slight enrichment in the liquid phase. In contrast, Figure 2c shows that Co, W, and Re are progressively depleted in the liquid, indicating their preferential incorporation into the solid phase and enrichment in dendritic cores. Cr and Fe also show mild segregation trends. To eliminate the segregation after solidification, solution heat treatment is essential. Homogenization processes serve to redistribute solute elements, dissolving undesirable secondary phases and reducing segregation. Heat treatment is a crucial process in controlling the microstructure and mechanical properties of HESAs. The specific heat treatment is designed for this HESA-X1 based on the Scheil solidification model and Differential Scanning Calorimetry (DSC) results (Setaram Labsys™, Lyon, Rhône, France), with the DSC data shown in Figure 3, to obtain microstructural uniformity.

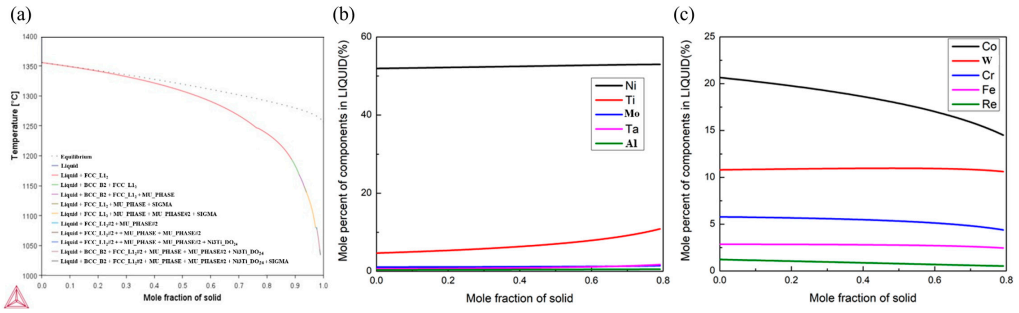

Figure 2. (**a**) Scheil simulation results for HESA-X1 alloy. (**b**) Elemental partitioning trends for elements (e.g., Re, Mo) exhibiting enrichment in the solid phase. (**c**) Partitioning behavior of elements (e.g., Al, Ti) that preferentially remain in the liquid phase.

The equilibrium phase diagram of the HESA-X1 alloy from Thermo-Calc simulation is presented in Figure 4a, indicating the formation of γ/γ', starting from nearly 1250 °C, and minor TCP phases such as σ and R phases at an intermediate temperature. The SEM backscattered electron micrograph of the as-cast HESA-X1 is presented in Figure 4b, showing a dendritic microstructure. To homogenize the segregation of HESA-X1, the temperature of the solid solution heat treatment was considered as 1275 °C for homogenization according to the Scheil simulation and the DSC result, and the γ' solvus temperature of HESA-X1 is 1242 °C. A fully homogenized microstructure achieved through solid solution heat treatment offers several critical advantages in HESAs, particularly in promoting microstructural stability and optimizing high-temperature mechanical performance. This process is especially crucial in multicomponent alloy systems, where solidification typically induces severe elemental segregation due to the disparate melting points and diffusion rates of constituent elements. Solid solution treatment facilitates long-range diffusion, enabling the redistribution of segregated solute atoms between dendritic and interdendritic regions [42–44]. This process effectively eliminates elemental segregation, resulting in a homogenized γ matrix with uniform chemical composition that serves as a stable foundation for subsequent

microstructural evolution. Figure 4c shows the fully homogenized microstructure after the solid solution heat treatment for HESA-X1. Such homogenization plays a critical role in governing the precipitation behavior of the $L1_2$-strengthened γ' phase during subsequent aging treatments. A homogenized γ matrix facilitates the uniform nucleation and growth of γ' precipitates, enabling precise control over their size, volume fraction, and morphology [45,46]. Microstructural uniformity is essential for optimizing strengthening mechanisms, thereby enhancing creep resistance and yield strength at elevated temperatures [47–49]. Furthermore, homogenization significantly suppresses the formation of TCP phases, which are often associated with localized segregation of refractory elements such as Re, W, and Mo. The formation of TCP phases adversely impacts ductility and creep life because of incoherency with the γ matrix and their inherent brittleness, which facilitates stress concentration in the surrounding regions [50]. A homogenized structure minimizes this risk by stabilizing solute distribution and suppressing the nucleation of undesirable phases. Achieving a homogenized microstructure ensures the reliability and reproducibility of subsequent heat treatments. Even minor compositional fluctuations in as-cast alloys can significantly influence phase transformation behavior during aging [51,52]. Thus, solid solution treatment is essential for maintaining microstructural consistency and achieving predictable property development in HESAs.

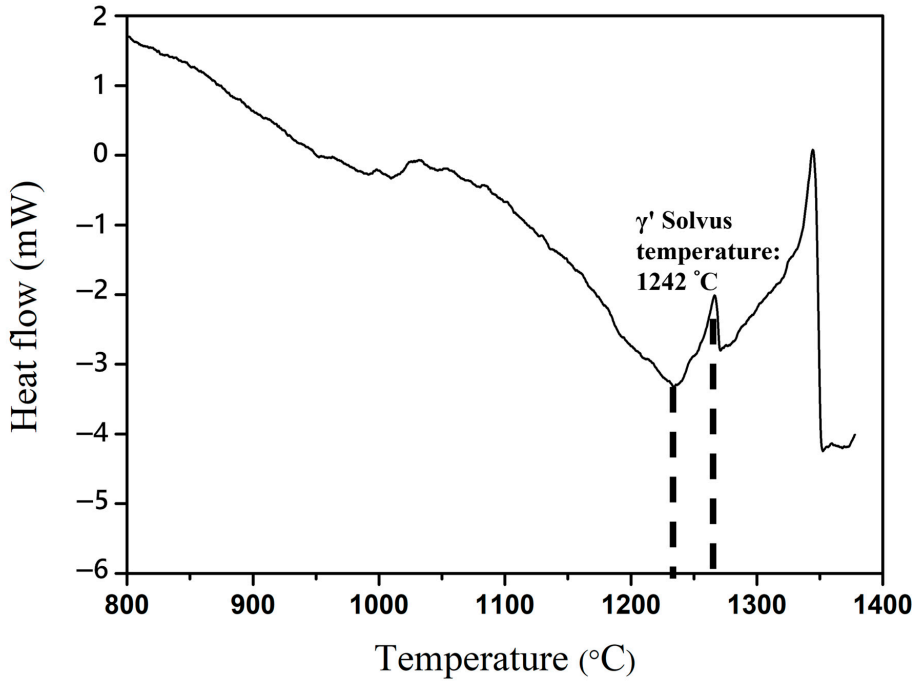

Figure 3. DSC cooling curve indicating the γ' solvus temperature of the alloy at approximately 1242 °C. The exothermic peak corresponds to the precipitation of the γ' phase during cooling.

Figure 4d indicates the last step of the setup of the starting microstructure in HESA-X1: a γ-γ' microstructure with a high fraction of γ' that was achieved after the heat treatment Ag-1. The uniform γ/γ' microstructure helps reduce internal stress concentrations and mitigates the initiation of creep damage [22]. The microstructure is characterized by dispersed cuboidal γ' precipitates with an average size of nearly 323 nm and a volume fraction of approximately 70%, suggesting a well-developed γ/γ' microstructure that contributes significantly to the high-temperature strength of the HESA-X1 alloy. This state will be the basis for all subsequent optimizations of the alloy in this work.

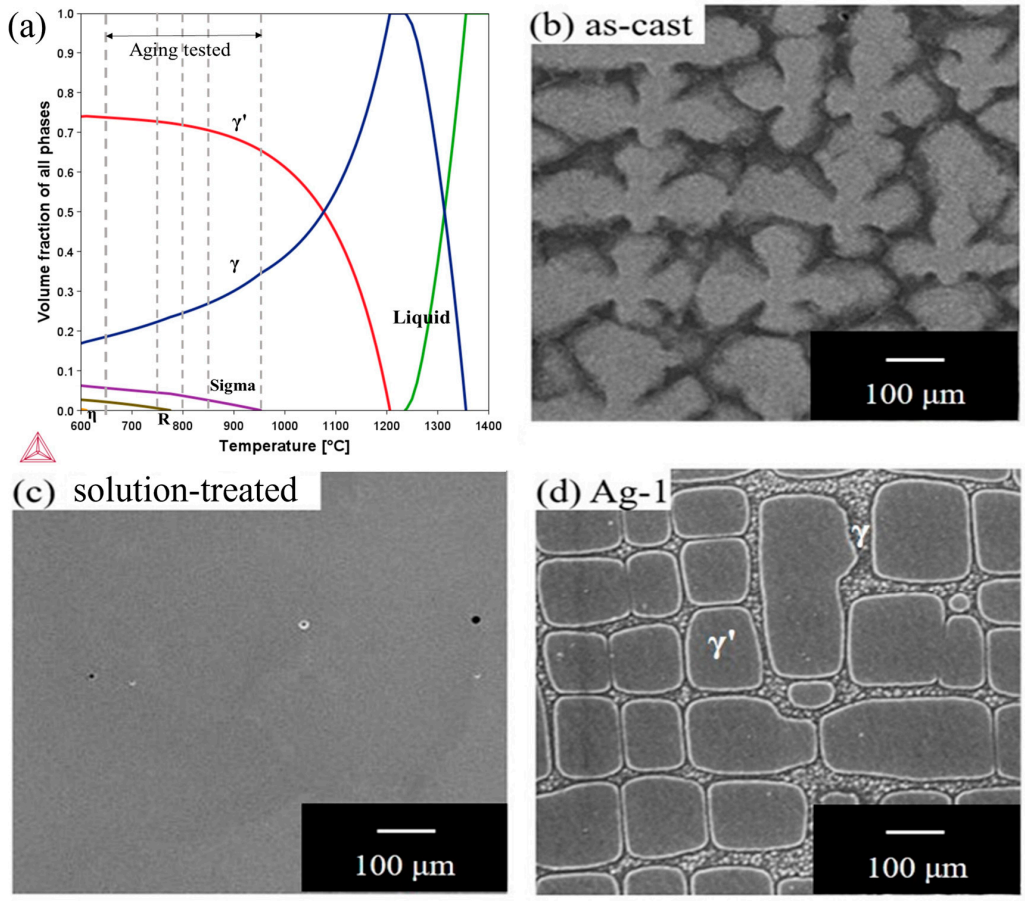

Figure 4. The microstructure of the HESA-X1 alloy: (**a**) the phase diagram calculated by Thermo-Calc with database TCHEA7 (the grey lines show the positions of heat treatments used in the study), (**b**) SEM micrograph of the as-cast microstructure, (**c**) SEM micrograph of the microstructure after solution heat-treatment at 1275 °C for 8 h, and (**d**) SEM micrograph of the microstructure after Ag-1 heat treatment.

The comprehensive investigation of the HESA-X1 alloy highlights the pivotal influence of elemental partitioning in governing microstructural evolution and mechanical performance. By integrating Scheil simulations with experimental validation, the study effectively elucidates the segregation behavior during solidification. Furthermore, the implementation of a tailored heat treatment strategy, developed based on simulation data and DSC analysis, demonstrates the efficacy of homogenization in alleviating compositional heterogeneities. The resultant optimized γ–γ' microstructure, characterized by a uniform dispersion of cuboidal γ' precipitates within the γ matrix following the Ag-1 heat treatment, as shown in Figure 4d, underscores the success of this approach.

3.2. Producing a Hierarchical Microstructure

HESAs can exploit the unique stoichiometric flexibility of their γ' phase to accommodate γ-forming elements under metastable conditions [26,29]. This can be achieved through rapid quenching followed by controlled aging, which facilitates the precipitation of γ-phase particles within the γ' matrix. Chen et.al [29] have shown that such a hierarchical microstructural strategy confers notable advantages for high-temperature performance. Specifically, the incorporation of intragranular γ particles within the γ' phase has been reported to retard coarsening kinetics [53], thereby enhancing microstructural stability. Moreover, this hierarchical architecture has been linked to improved compression creep life at elevated temperatures [54]. Consequently, the implementation of hierarchical mi-

crostructure design in HESAs represents a promising route toward achieving superior high-temperature mechanical properties. This approach offers a cost-effective alternative to traditional strategies that rely on high concentrations of costly refractory elements, enabling further strengthening through microstructural optimization alone.

The optimum formation temperature for the γ particles inside γ′ is tested over a range from 450 to 950 °C for the HESA-X1. The reference microstructure shown in Figure 4d, namely Ag-1, has no internal γ particles. The aging duration for internal γ formation is set at 20 h, which was taken from previous works [29]. Figure 5 presents the microstructures observed by SEM. Based on Image J analysis, the γ′ precipitates exhibit a uniform size distribution, and the γ particles are approximately 6 nm in size. To design an effective aging strategy for promoting the formation of γ particles within γ′ precipitates, the parameters were guided by the work of Gorsse et al. [55]. Their study systematically explored the hierarchical precipitation behavior in a similar SX HESA system (HESA-3), using both computational modeling and experimental validation to identify optimal aging temperatures and durations. Drawing from these insights, the current study applies analogous aging protocols to investigate hierarchical microstructure evolution in HESA-X1. By establishing the optimized size and volume fraction of precipitations during thermal treatments, their findings provide a reliable basis for designing aging parameters that enhance high-temperature performance. Accordingly, the heat treatment parameters in this study were established based on the findings of Gorsse et al. [55], whose work demonstrated the formation of a hierarchical γ–γ′–γ architecture. Their heat treatment design served as a reference standard for exploring similar phase evolution behavior in the present alloy system.

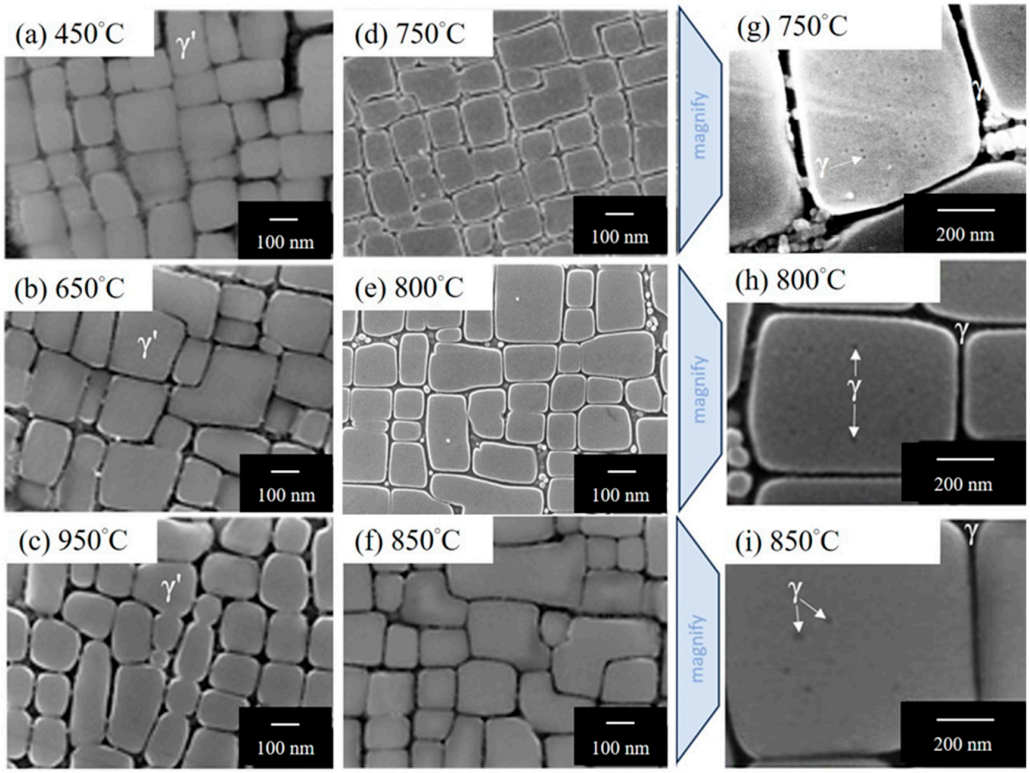

Figure 5. SEM images of the evolution of γ′ morphology in the HESA-X1 under various aging temperatures for 20 h. (a–f) represent the general γ/γ′ microstructure at different temperatures: (**a**) 450 °C, (**b**) 650 °C, (**c**) 950 °C, (**d**) 750 °C, (**e**) 800 °C, and (**f**) 850 °C. (**g**–**i**) are magnified views of γ′ precipitates within the γ matrix from (**d**–**f**), highlighting the formation of γ particles within the γ′ phase for (**g**) 750 °C, (**h**) 800 °C, and (**i**) 850 °C.

The formation of γ particles in the HESA-X1 alloy was systematically investigated following the Ag-1 heat treatment and subsequent aging at various temperatures for 20 h, as shown in Figure 5. After aging at 450 °C, 650 °C, and 950 °C, no γ particles were observed within the γ′ matrix, indicating that the thermal conditions at these temperatures are either insufficient or unfavorable for γ particle precipitation. In contrast, at 750 °C, 800 °C, and 850 °C, γ particles began to appear, as clearly revealed in the magnified images (Figure 5g–i). The γ particles were observed to precipitate within the γ′ matrix, suggesting that their formation is highly temperature-dependent and becomes favorable in the intermediate temperature range of 750 to 850 °C. Subsequently, as shown in Figure 6, Vickers hardness measurements were performed to identify the aging temperature that yields the highest strength, with all aging treatments conducted for 20 h. The results indicate that the peak hardness was achieved after aging at 750 °C for 20 h. Therefore, the aging treatments consisting of 1100 °C for 2 h, followed by air cooling, and 750 °C for 20 h, followed by water quenching after solution heat treatment, are designated as Ag-2 in this study.

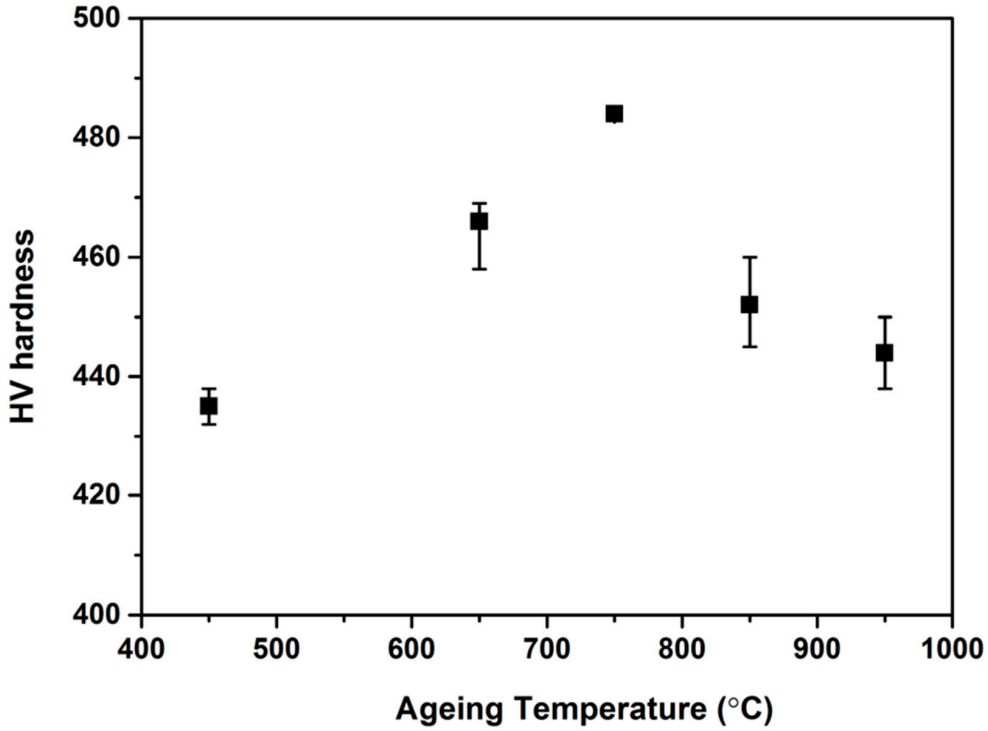

Figure 6. Vickers hardness of the HESA-X1 alloy as a function of aging temperature after Ag-1 treatment. All aging treatments were conducted for 20 h.

To further confirm the identity and crystal structure of the precipitates formed under the Ag-2 condition, TEM dark-field imaging and selected area diffraction pattern (SADP) were performed. The results indicate that the cuboidal precipitates possess an $L1_2$-ordered structure in the Ag-2 state. The contrast between $L1_2$ phases (brighter contrast), the FCC matrix (dark contrast), and nanoparticles (dark contrast) are distinguishable from the dark-field image (Figure 7) obtained from the (001) superlattice reflection spot of $L1_2$ (as indicated in the SADP obtained along the [001] zone axis of $L1_2$ in the inset of Figure 7). In addition, diffraction spots corresponding to the [001] zone axis of FCC are visible. In addition, a cube-on-cube orientation relationship between the FCC and $L1_2$ phases is clearly observed, with $[100]_{FCC} \| [100]_{L12}$ and $[010]_{FCC} \| [010]_{L12}$, indicating the presence of perfectly coherent interfaces. Combining the results of dark field images and the diffraction pattern, it could be concluded that the phase structure of nanoparticles is the same as that of the

matrix, which corresponds to the disordered FCC γ phase. Therefore, the Ag-2-treated HESA-X1 presents nanoparticles dispersed within cuboidal $L1_2$ precipitates. Namely, the Ag-2 treated HESA-X1 presents the matrix–precipitate–particle hierarchical microstructure consisting of nanoparticles dispersed within primary cuboidal precipitates (Figure 5g), which is not observed in Ag-1. In addition, the Ag-1 condition exhibited an average $L1_2$ phase size of 329 nm and a volume fraction of 69.8%, while the Ag-2 condition showed a comparable $L1_2$ phase size of 330 nm and a volume fraction of 70.2%, as measured from SEM images using Image J. These results indicate that the two aging treatments, Ag-1 and Ag-2, produced nearly identical γ′ morphologies.

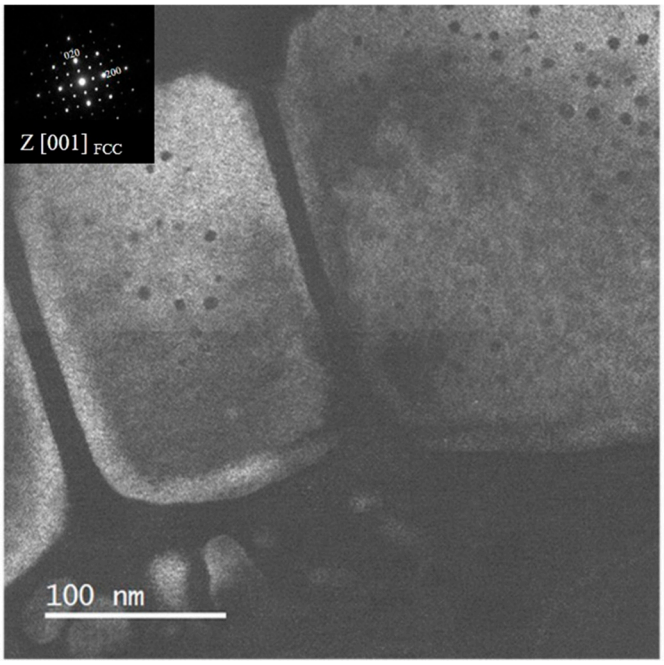

Figure 7. TEM dark field image of the Ag-2 sample from $L1_2$ (001) superlattice spot on [001] zone axis for the HESA-X1.

To further investigate the compositional distribution at the near-atomic scale, APT was conducted on the Ag-2 aged sample. The reconstructions were utilized to verify the phase distribution of HESA-X1 post Ag-1 and Ag-2 treatments. Cr-8 at.% iso-surface was established at the interface between the FCC matrix–$L1_2$ precipitate for distinction with the laser mode. As shown in Figure 8a, the γ matrix and dispersed γ′ precipitates are observed in HESA-X1 post Ag-1 treatment. On the other hand, the Ag-2 treated HESA-X1-present γ-γ′-γ hierarchical microstructure consists of FCC γ nanoparticles formed inside $L1_2$ γ′ precipitates, which are embedded in the FCC γ matrix (Figure 8b). This is consistent with the results observed from SEM images shown in Figure 5g–i. Furthermore, 1D concentration profiles extracted across the γ′/γ interface are shown in Figure 8c,d, corresponding to the regions of interest (ROI-1, ROI-2, and ROI-3) marked in Figure 8a,b. The concentration profiles provide detailed information on the local elemental compositions across the γ′/γ interface, revealing significant differences in the distribution of individual alloying elements. Notably, elements such as Ni, Al, and Ti are enriched in the γ′ phase, whereas Co, Cr, and Re are concentrated in the γ matrix, indicating pronounced partitioning behavior. A quantitative summary of both elemental concentrations and partitioning coefficients is presented in Tables 2 and 3.

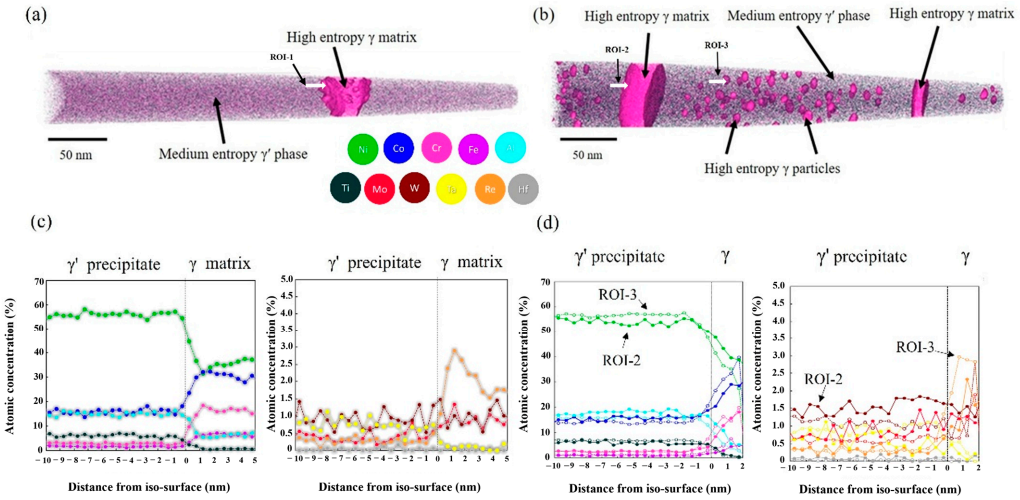

Figure 8. APT reconstructions of the HESA-X1 alloy after (**a**) Ag-1 and (**b**) Ag-2 heat treatments. Regions of interest (ROIs) for 1D concentration profiles were selected across the γ'/γ interface. (**c**) and (**d**) show the 1D concentration profiles of major (**left**) and minor (**right**) alloying elements. (**c**) corresponds to ROI-1 in the Ag-1 condition, while (**d**) corresponds to ROI-2 and ROI-3 in the Ag-2 condition. Cr-8 at.% is set as iso-surface.

Table 2. The composition of different phases analyzed by APT and the calculated partitioning coefficients (Pi) for the HESA-X1 after Ag-1 heat treatment.

HESA-X1 (at.%)	Al	Ti	Cr	Fe	Co	Ni	Mo	Re	W	Ta	Hf
Nominal	12	5	6	3	20	50.87	0.5	1	1	0.6	0.03
FCC γ matrix	5.7	0.77	15.9	5.2	31.2	36.6	0.98	2.34	1.02	0.29	0
$L1_2$ γ′ precipitate	15.1	7.73	2.2	2.15	17.6	52.7	0.38	0.42	0.98	0.74	0
Pi (γ matrix/γ′)	0.38	0.1	7.22	2.42	1.77	0.69	2.58	5.57	1.04	0.39	-

Table 3. The composition of different phases analyzed by APT and the calculated partitioning coefficients (Pi) for the HESA-X1 after Ag-2 heat treatment.

HESA-X1 (at.%)	Al	Ti	Cr	Fe	Co	Ni	Mo	Re	W	Ta	Hf
Nominal	12	5	6	3	20	50.87	0.5	1	1	0.6	0.03
FCC γ matrix	5.5	0.59	16.7	3.3	30.3	38.28	1.08	2.58	1.44	0.23	0
FCC γ particles	4.3	0.41	16.89	3.58	31.83	38.01	0.83	2.75	1.05	0.35	0
$L1_2$ γ′ precipitate	17.3	7.46	2.9	2.1	16.1	51.02	0.85	0.34	1.18	0.75	0
Pi (γ matrix/γ′)	0.32	0.08	5.76	1.6	1.88	0.76	1.27	7.56	1.22	0.31	-
Pi (γ particles/γ′)	0.25	0.05	7.34	1.7	1.98	0.75	1.3	8.01	1.37	0.47	-

To confirm the reliability of the results for the APT, the mass balance of lever rule should be calculated. Therefore, the volume fraction of γ′ phase (fγ′) in HESA-X1 was computed by the level rule formula:

$$\mathrm{Cm} = \mathrm{f}\gamma\prime C_i^{\gamma'} + (1 - \mathrm{f}\gamma\prime)C_i^{\gamma} \quad (1)$$

where Cm, $C_i^{\gamma'}$, and C_i^{γ} are the concentrations of each alloyed element in the overall material, γ′ and γ phases, respectively. Figure 9 shows the volume fraction of γ′ phase within aged HESA-X1 calculated from the APT result. The volume fraction of γ′ phase obtained from APT is about 0.72, which is nearly the same as that calculated by Image J via SEM images (~0.70). The result emphasizes the reliability of APT analysis in the present study, although it may be noted that the field of view is extremely limited in APT

analysis when compared to that of SEM imaging. Therefore, the hierarchical microstructure obtained by Ag-2 treatment could be regarded as a γ-γ′-γ hierarchical microstructure, which is consistent with that reported in a previous study [29]. In addition, the lattice misfit between the γ matrix and the $L1_2$ γ′ precipitate was calculated by the diffraction pattern of TEM results, and the value of misfit is 0.0027 for HESA-X1, which is considered as a beneficial value for mechanical properties and phase stability [56–58].

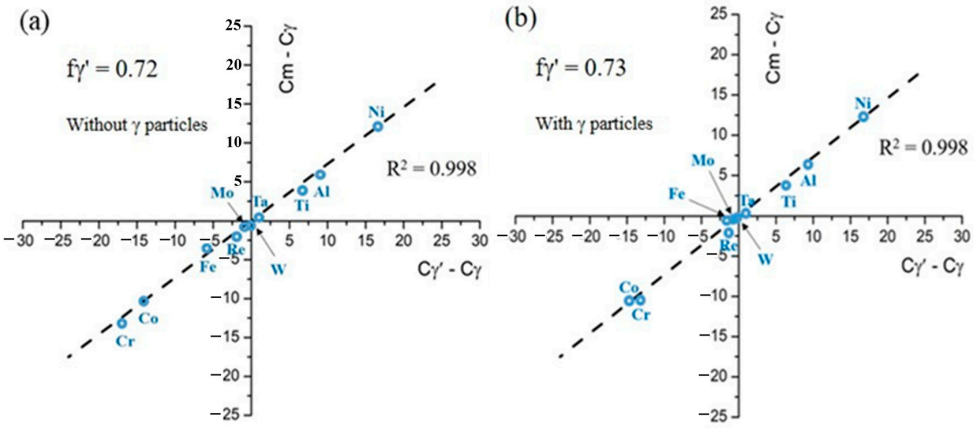

Figure 9. The plot of Cn-Cγ vs. Cγ′-Cγ derived from compositions of HESA-X1 alloys by APT analysis with (**a**) Ag-1 heat treatment and (**b**) Ag-2 heat treatment.

In addition to the microstructural evolution of the HESA-X1 alloy, the partitioning behavior between constituent phases represents another critical factor. The elements in HESAs exhibit distinct partitioning tendencies that are fundamental to alloy design. Elements such as Al and Ti preferentially partition into the γ′ precipitates, while Co, Cr, and Fe are enriched in the γ matrix, as shown in Figure 8. These partitioning behaviors have a pronounced impact on both the thermodynamic and mechanical stability of the alloy. In particular, the configurational entropy of each phase within the γ matrix and the γ′ precipitates are governed by the distribution of constituent elements. To fully exploit the benefits of the high-entropy alloy concept, it is essential to maintain a high-entropy state in the γ matrix and at least a medium-entropy state in the γ′ phase, thereby ensuring optimal thermal stability.

The partitioning coefficient *Pi*, which quantifies the distribution of elements between phases, serves as a critical parameter for characterizing lattice misfit and even correlating with creep behavior. It is defined by the following equation: $Pi = C_i^{\gamma} / C_i^{\gamma'}$, where C_i^{γ} and $C_i^{\gamma'}$ are the concentration of elements in the FCC matrix and in the $L1_2$ phase obtained from APT analysis, respectively. Typically, elements such as Al, Ti, Nb, Ni, and Ta in HESA-X1 tend to partition into the $L1_2$ phase during aging, as indicated by their partitioning coefficients being less than unity. In contrast, elements such as Co, Cr, Fe, Mo, W, and Re preferentially diffuse toward the FCC γ matrix, exhibiting partitioning coefficients greater than one. As shown in Figure 10, the partitioning behavior was quantified based on previous APT analyses of the HESA-X1 alloy after Ag-1 and Ag-2 heat treatments. The results reveal partitioning coefficients for Al, Ti, Ta, and Ni of 0.38, 0.10, 0.39, and 0.69, respectively, confirming their strong affinity for the $L1_2$ γ′ precipitates. Conversely, Co, Cr, Fe, Mo, W, and Re exhibit coefficients of 1.77, 7.22, 2.42, 2.58, 1.04, and 5.57, respectively, indicating their preferential enrichment in the γ matrix. A similar partitioning trend is also observed between the γ nanoparticles and γ′ phase, further confirming the consistent behavior across γ/γ′. Additionally, it presents the partitioning coefficients for γ-forming elements such as W and Re after Ag-2 treatment. The coefficients are 1.22 for W and 7.56 for Re, which demonstrate the diffusion of certain γ-forming elements from the $L1_2$ γ′ precipitates to form

the γ phase, leading to the formation of γ particles after the second step of aging within the Ag-2 process. Notably, the partitioning coefficient of Re in HESA-X1 is significantly lower than those reported for Ni-based superalloys [59]. This suggests a distinct discrepancy in the partitioning behavior of Re between the γ matrix and γ′ phase in HESA-X1. After the Ag-1 heat treatment, the γ′ phase remains in a supersaturated state, enriched with refractory elements. Upon subsequent Ag-2 treatment, γ nanoparticles nucleate within the supersaturated γ′ phase. The high concentration of refractory elements, particularly Re, detected within these γ nanoparticles, indicates that HESA-X1 can incorporate a greater number of γ-forming elements within its γ′ phase following Ag-1 heat treatment, compared to conventional superalloys. These findings underscore the dynamic redistribution of elements under tailored heat treatment conditions and highlight the critical role of Re in facilitating γ particle formation.

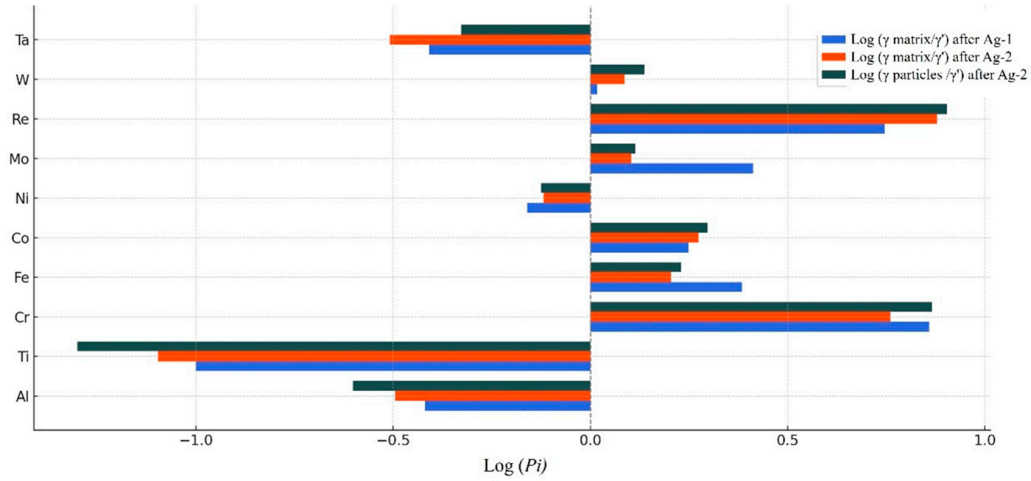

Figure 10. Partitioning behavior of elements between the FCC γ matrix and the $L1_2$ γ′ phase, as well as between γ particles and the γ′ phase, in the HESA-X1 alloy after Ag-1 and Ag-2 heat treatments.

3.3. Stability of the Microstructure

The phase stability of HESAs is a critical factor that directly influences their mechanical performance, microstructural integrity, and long-term reliability in severe service environments. Among the alloying elements, Re is well known for its beneficial contributions to high-temperature phase stability [60]. Re enhances solid solution strengthening within the γ matrix, thereby increasing resistance to dislocation motion [61,62]. In addition, Re significantly suppresses the coarsening and dissolution of γ′ precipitates by reducing atomic mobility, thereby enhancing the stability of the γ/γ′ two-phase microstructure during prolonged high-temperature exposure [63]. It inhibits diffusion-controlled creep mechanisms, particularly under conditions where lattice diffusion is dominant, leading to improved creep resistance. Consequently, instabilities such as γ′ coarsening, dissolution, or phase transformation can severely degrade mechanical performance and must be carefully considered in the design and application of HESAs.

Chen et al. [29] developed the HESA with a γ–γ′–γ hierarchical microstructure. However, the hierarchical γ-γ′-γ structure is in a metastable state, which means that the γ nanoparticles easily re-dissolve back into the γ matrix at elevated temperatures. Thus, it will be detrimental to the time-dependent mechanical properties, such as creep performance. These results highlight that a clear understanding of the correlation between heat treatment history and the thermodynamic driving forces for phase precipitation is essential for the microstructural optimization of HESAs. Therefore, the HESA-X1 with a γ-γ′-γ hierarchical microstructure is produced for better phase stability compared to the previous work [29]. To study the phase stability of FCC γ nanoparticles at higher

temperatures, aging after Ag-2 treatments was additionally performed on HESA-X1 at 750 °C, 800 °C, and 850 °C for 20, 100, and 200 h. The resultant microstructures are shown in Figure 11. SEM images in SE mode show that FCC γ nanoparticles still existed in γ′ phase after exposure at 750 °C, 800 °C, and 850 °C from 20 to 200 h for the HESA-X1. At 750 °C for 20 h (Figure 11a), the γ′ precipitates exhibit sharp interfaces and a distinct size contrast between the primary γ′ phase and the embedded γ nanoparticles. As the aging duration increases to 100 and 200 h (Figure 11b, c), the γ′ morphology remains coherent, and only slight coarsening of the γ particles is observed. A similar trend is observed at 800 °C (Figure 11d–f), where both the γ′ phases and the γ particles show gradual coarsening with time. At 850 °C (Figure 11g–i), the γ′ precipitates maintain their cuboidal morphology up to 200 h, indicating strong thermal resistance. Although minor rounding at the corners is observed at prolonged aging times, the γ–γ′–γ hierarchical structure remains largely intact. Moreover, with the measurement of size and volume fraction using SEM image analysis, the size of FCC γ particles is nearly the same as that of the Ag-2 treatment. However, the previous study showed that there are almost no FCC γ particles observed in Re-free HESA alloy aged at 750 °C for 200 h [29]. These results prove that HESA-X1 has more stable γ particles compared to those in Re-free HESA. The underlying mechanism is related to the addition of Re, which can reduce the diffusion kinetics of the atoms and hinder the diffusion of elements between γ and γ′ phases at high temperatures. In addition, SEM analyses detected no TCP phases under any heat treatment condition. Figure 12 displays the XRD patterns for the as-cast alloy, after Ag-2 aging, followed by additional heat treatment at 850 °C for 200 h, all indicating the presence of γ and γ′ phases only and confirming the superior phase stability of HESA-X1.

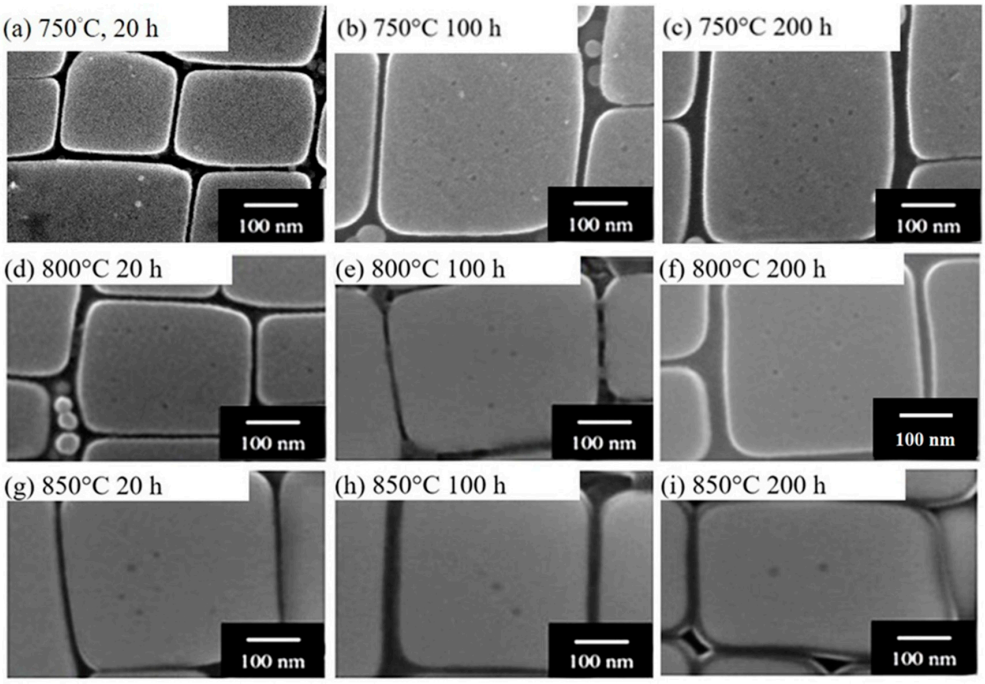

Figure 11. SEM observations of HESA-X1 alloys are exposure at 750 °C, 800 °C, and 850 °C from 20, 100, and 200 h after Ag-2 aging heat treatment.

After confirming the phase stability of γ nanoparticles, Figure 13 presents the creep curves of HESA-X1 with (after Ag-2) and without (after Ag-1) γ particles under creep conditions of 760 °C and 600 MPa. As shown in Figure 13, the presence of γ particles clearly enhances the creep life of HESA-X1, indicating their significant role in improving creep resistance. To elucidate the underlying mechanisms of the strengthening effect and to address the issue of excessive creep strain, further investigations should be conducted,

including detailed dislocation analyses using TEM or molecular dynamics (MD) simulations. These results will help to clarify how dislocations interact with γ nanoparticles and provide insights for the future optimization of HESAs.

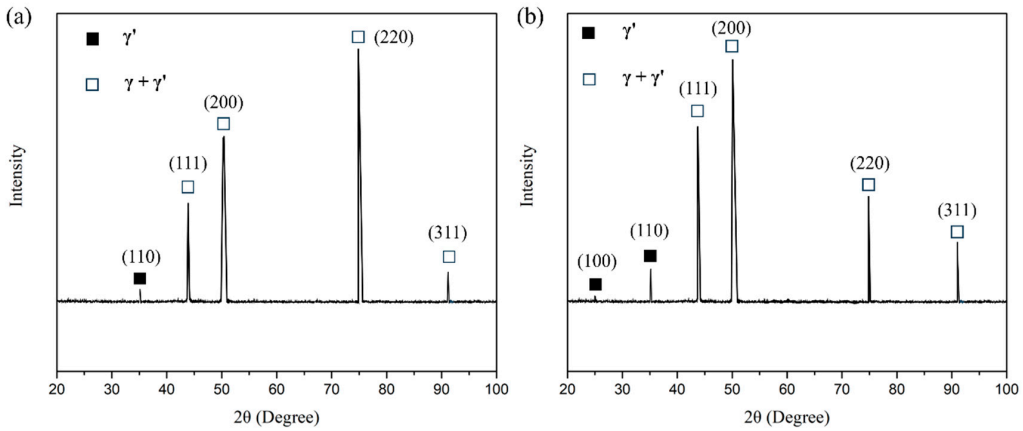

Figure 12. XRD patterns of the HESA-X1 alloy showing γ′ and γ + γ′ phases: (**a**) as-cast condition and (**b**) after Ag-2 treatment followed by additional aging at 850 °C for 200 h. The diffraction peaks correspond to the γ′ phase (solid squares) and overlapping γ + γ′ phases (open squares).

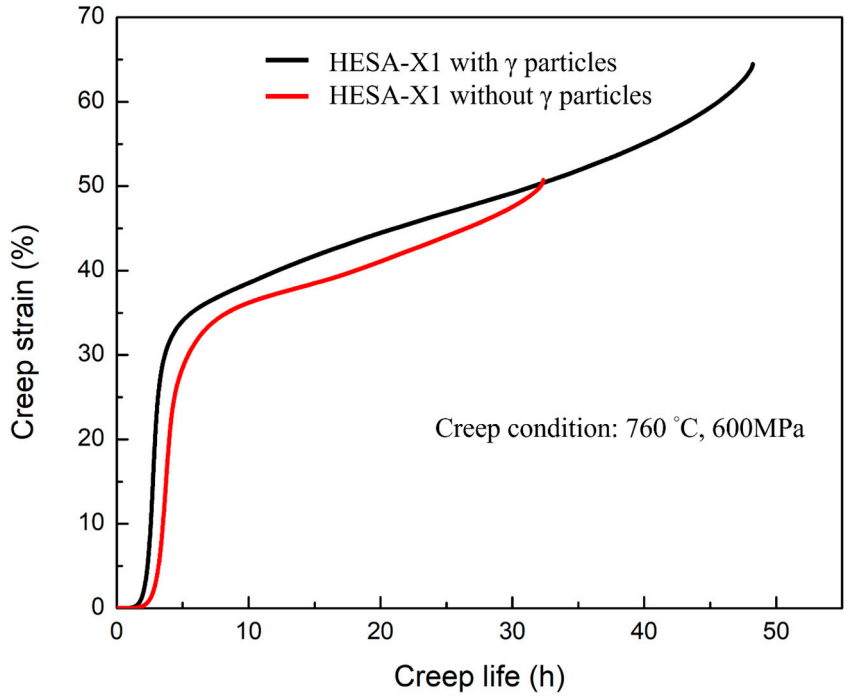

Figure 13. Creep curves of the HESA-X1 alloy with and without γ particles tested at 760 °C under an applied stress of 600 MPa.

While the previous SEM observations qualitatively confirmed the morphological stability of the γ′ precipitates, a quantitative evaluation of their coarsening behavior is essential for assessing their long-term performance under thermal exposure in the severe environment, such as at elevated temperatures up to 850 °C. The change of morphology, size, and volume fraction of γ′ precipitates resulted from the exposure of high temperatures and/or stresses are highly related to the mechanical properties of alloys [64–67]. For example, cuboidal shape γ′ precipitates are more preferred for mechanical properties such as creep resistance than spherical γ′ precipitates [65]. In Figure 11, the γ′ phase in HESA-X1 maintained a cuboidal shape with only minor coalescence even exposed at 850 °C for 200 h. These results indicate that the HESA-X1 alloy has remarkable γ′ phase stability. It is an

identical result with the phase stability of FCC γ nanoparticles. In general, the coarsening of the γ′ is characterized by the classical Lifshitz–Slyozov–Wagner (LSW) model [34,35,68,69], which is the most used model for the calculation of phase coarsening during aging heat treatments [70,71]. The formula for the LSW model is as follows:

$$r_t^3 - r_0^3 = Kt \quad (2)$$

where r_t is the mean radius of γ′ precipitates at aging time t, r_0 is the mean radius of γ′ phase at t = 0, and K is the coarsening rate constant.

The coarsening rate K of γ′ precipitates at specific temperatures has a tremendous impact on the performance of alloy components. In the present work, the Re element was added to HESA-X1 for the inhibition of γ′ coarsening. The specimens were first treated by Ag-1 and then underwent extra aging treatments at different temperatures of 450 °C, 650 °C, 750 °C, 800 °C, and 850 °C isothermally for 50, 100, and 200 h to study the coarsening of γ′ precipitations. The microstructure of HESA-X1 post-Ag-1 aging treatment, shown in Figure 4d, is set as the benchmark. The evolution of the morphology of γ′ precipitates during extra aging from 450 to 850 °C is shown in Figure 14. It reveals that the γ′ precipitates coarse with respect to aging temperature and time. A lower K value in the LSW coarsening model indicates a significantly reduced coarsening rate of γ′ precipitates. Since K is directly proportional to the diffusivity of solute atoms, a lower value suggests sluggish diffusion, typically due to the presence of slow-diffusing refractory elements such as Re [72,73]. This reduction in coarsening kinetics helps maintain the fine and uniform distribution of γ′ precipitates over long-term thermal exposure, thereby preserving the alloy's strength and creep resistance at elevated temperatures. In high-temperature applications, minimizing γ′ coarsening is crucial for sustaining the microstructural integrity and mechanical performance of HESAs.

The simulated temporal evolution of γ′ and γ particle sizes in the HESA-X1 alloy highlights a distinct hierarchical growth behavior. As shown in Figure 15, γ′ precipitates exhibit rapid growth, while γ particles nucleate and grow at a much slower rate during prolonged aging. This kinetic disparity reflects the formation of a stable γ–γ′–γ microstructure, which plays a crucial role in maintaining microstructural integrity during high-temperature service. Notably, the predicted size of γ′ precipitates from the simulation closely aligns with the experimental measurements obtained from SEM analysis after Ag-1 treatment. However, the predicted γ particle size shows limited agreement with the experimental values obtained from SEM analysis after Ag-2 treatment. This discrepancy may arise from the relatively large measurement errors associated with Image J when analyzing particles with dimensions at the nanoscale. Nevertheless, both the predicted and measured values for the γ particles remain within the same order of magnitude, indicating that the simulation still provides a valuable reference for understanding their coarsening behavior. In addition, according to Gorsse et al. [35], the γ particles in the Re-free HESA-3 alloy reached a size of approximately 2 nm after aging at 750 °C for 10 h and grew to around 4 nm after 20 h. In contrast, the γ particles in the Re-bearing HESA-X1 alloy exhibited a size of approximately 4 nm after 10 h and about 6 nm after 20 h under the same aging conditions. The particle sizes were quantitatively determined from SEM images. The findings demonstrate that the γ particles in the Re-bearing HESA-X1 alloy exhibit enhanced thermal stability and reduced coarsening compared to those in the Re-free HESA-3 alloy.

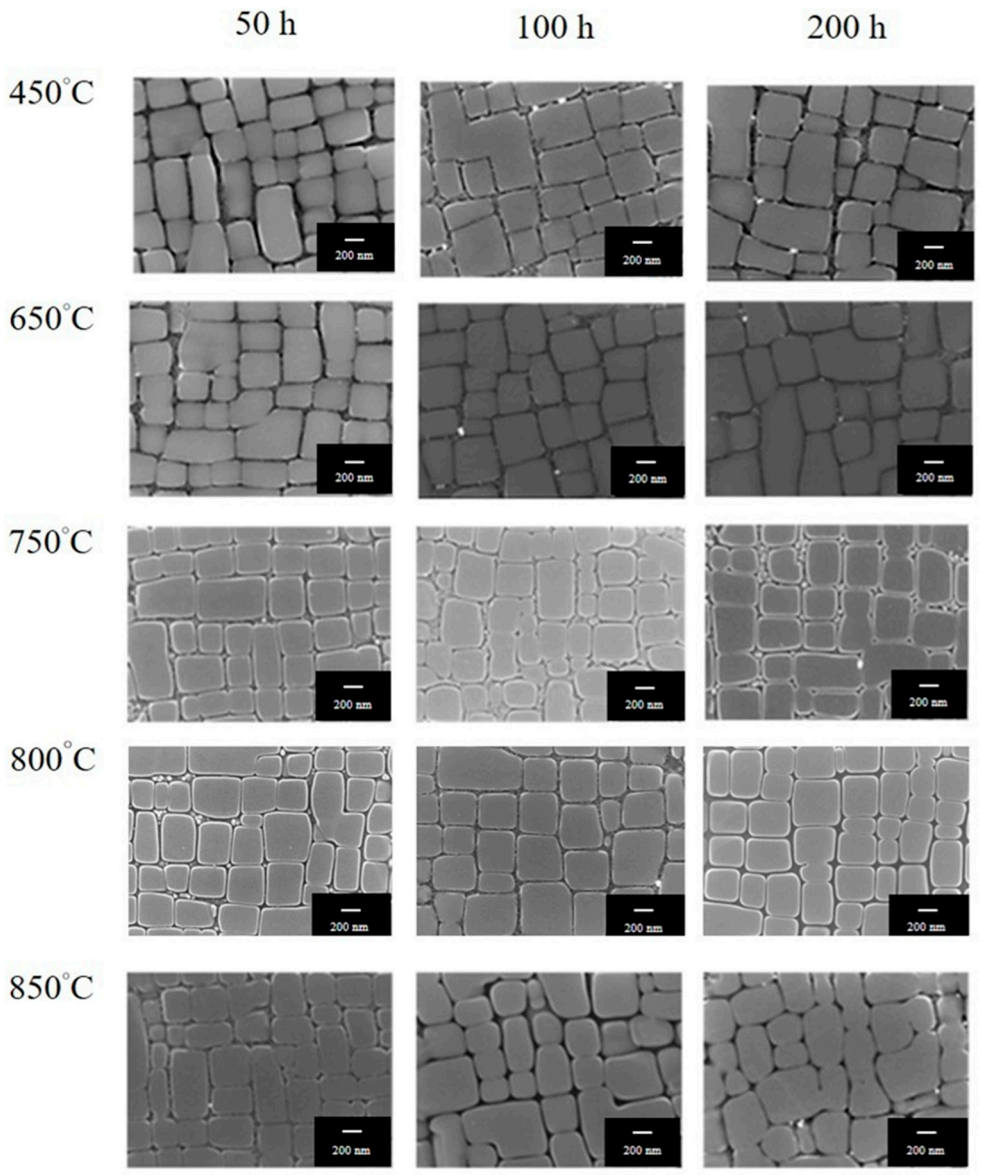

Figure 14. Evolution of the morphology of γ′ precipitates within HESA-X1 alloys during extra aging from 450 to 850 °C with 50, 100, and 200 h of SEM observations after Ag-1 aging treatment.

To rigorously validate the coarsening behavior, experimental analysis and quantitative evaluation based on the LSW model were conducted using SEM images processed via Image J (Bethesda, MD, USA). For example, the coarsening behaviors of HESA-X1 were evaluated at 750 °C for 50 h, 100 h, and 200 h. The average γ′ precipitate size increased only slightly, from 329 nm in the initial condition (after Ag-1) to 330 nm after 50 h, 331 nm after 100 h, and 333 nm after 200 h, corresponding to a calculated coarsening rate constant K of approximately 1.83 (nm^3/s). This relatively low value indicates excellent microstructural stability and suppressed coarsening kinetics. Conversely, the γ′ precipitate size in the Re-free HESA (HESA-3) alloy grew markedly at 750 °C, enlarging from 143 nm to roughly 170 nm after 100 h, and reaching around 190 nm after 200 h [55]. The corresponding K value was calculated to be 5.47 (nm^3/s) at 750 °C, which is three times higher than that of HESA-X1. A lower K value implies that the mean radius of γ′ precipitates after extended aging (t = 50 h, 100 h, and 200 h) remains close to that after the Ag-1 (HT-1 [29]) treatment (t = 0), thereby confirming the higher microstructural stability of HESA-X1 than HESA-3. Figure 16 presents plots of ($r^3 - r^0$) versus time for HESA-X1 (Figure 16a) and HESA-3 (Figure 16b), measured at 750 °C. For HESA-X1, measurements were taken at

0 h, 50 h, 100 h, and 200 h, whereas for HESA-3, data were collected at 0 h, 100 h, and 200 h. The results also clearly indicate that the constant K for HESA-X1 is lower than that of HESA-3. It should be emphasized that the y-axes of Figure 16a,b differ by one order of magnitude, which makes the slope in Figure 16b appear smaller. The slope in Figure 16a is approximately one-third of that in Figure 16b.

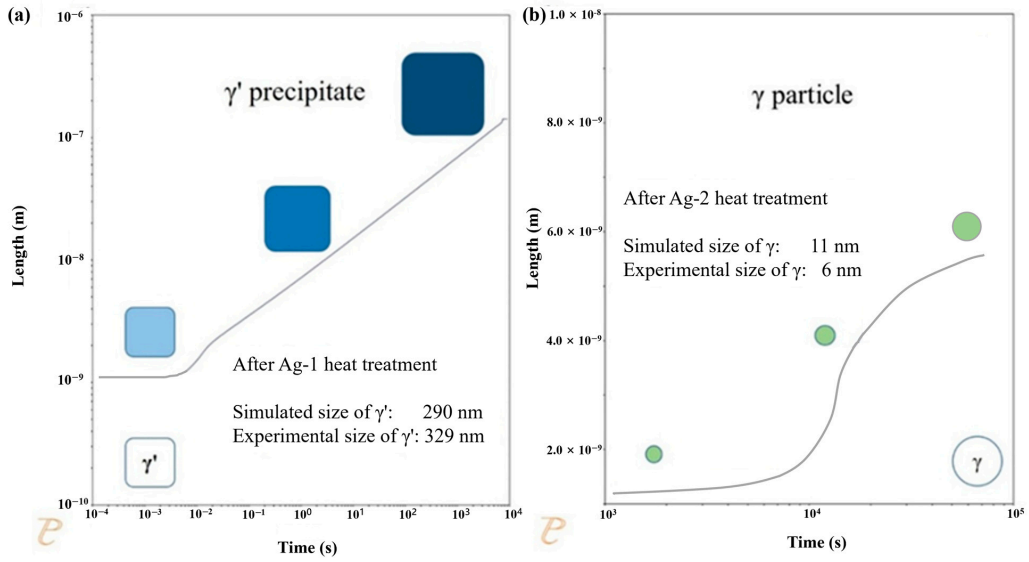

Figure 15. Simulated time-dependent evolution of (**a**) γ′ precipitate and (**b**) γ particle sizes in the HESA-X1 alloy, as predicted by TC-PRISMA (using the thermodynamic database TCHEA7 and the kinetics database MOBHEA2) and compared with experimental measurements. Both Y-axes represent precipitate radius (in meters) on a logarithmic scale, while the X-axes indicate time, also on a logarithmic scale. All plotted shapes and curves represent simulation results only, and the shapes do not represent actual sizes. Experimental values are shown solely as annotated size labels for reference and are not plotted as data points.

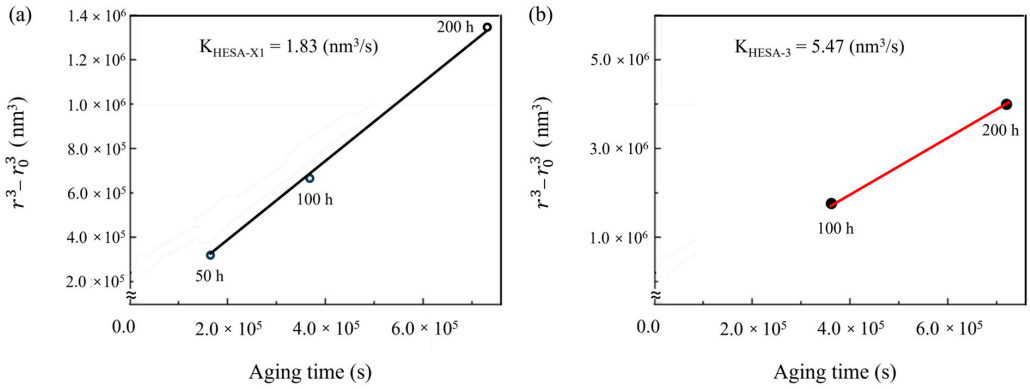

Figure 16. ($r^3 - r_0^3$) vs. time plots at 750 °C for (**a**) HESA-X1 and (**b**) HESA-3.

In addition to the LSW model, the Trans-Interface Diffusion-Controlled (TIDC) model is also employed to evaluate coarsening behavior, particularly when interfacial diffusion is the dominant mechanism [74–76]. This model is commonly applied to systems undergoing early-stage coarsening, where interfacial diffusion processes dominate the kinetics. To determine the most appropriate model for the present study, both approaches were examined. The nearly constant coarsening rate constant K obtained from the LSW model, along with the minimal variation in γ′ precipitate size, suggests that the coarsening behavior is more accurately described by the LSW model. In contrast, the TIDC model produced slightly fluctuating K values across different aging times, indicating that bulk diffusion, rather than interfacial diffusion, governs the coarsening kinetics under the current aging

conditions. This observation is further supported by the presence of a slow-diffusing refractory element such as Re [77], which significantly hinders atomic mobility within the γ matrix and thereby favors diffusion-controlled coarsening as predicted by the LSW model. It significantly reduces the effective diffusivity of solute atoms, thereby retarding the migration of atoms and slowing the coarsening kinetics. The consistently low and relatively temperature-insensitive K further confirms that Re additions effectively suppress diffusion-controlled coarsening kinetics. This conformity indicates that the rate-limiting step for γ' coarsening is governed by the diffusion of the slowest-moving solute species within the γ matrix. These results indicate that the incorporation of Re effectively stabilizes both the fine γ nanoparticles and the $L1_2$-structured γ' precipitates, mitigating coarsening even under prolonged thermal exposure. Namely, the superior coarsening resistance in HESA-X1 is primarily attributed to the presence of Re, the element with an extremely low diffusion coefficient in the γ matrix. As a result, the γ' precipitates in HESA-X1 remain stable over long-term thermal exposure, ensuring enhanced microstructural integrity and mechanical reliability. These findings provide compelling evidence that the addition of Re is a highly effective strategy to improve phase stability in high-entropy superalloys. By limiting atomic mobility, Re not only suppresses γ' coarsening but also contributes to the development of thermally stable alloy systems for high-temperature applications.

This study affirms that in HESA-X1, the element with the lowest diffusivity, typically Re, acting as the rate-limiting factor for diffusion-controlled processes, is the main reason for the improved phase stability. This understanding is crucial for the design and optimization of HESAs intended for high-temperature applications, where microstructural stability is paramount. Moving forward, the integration of kinetic simulations, such as TC-Prisma, is essential to accurately predict the temporal evolution of γ' precipitate and γ particles' size and fraction. Such modeling will aid in optimizing heat treatment strategies and tailoring the phase morphology for superior mechanical performance.

4. Conclusions

This study presents the successful development and characterization of the SX Re-bearing HESA-X1 with a thermally stable hierarchical γ–γ'–γ microstructure. The following conclusions can be drawn.

(1) Through a two-step aging treatment (Ag-2), HESA-X1 exhibits a refined hierarchical structure composed of FCC γ nanoparticles embedded within $L1_2$-ordered γ' precipitates, themselves uniformly distributed in an FCC γ matrix. This hierarchical γ–γ'–γ microstructure enhances high-temperature mechanical stability, resists microstructural degradation under prolonged thermal exposure, and improves mechanical properties.

(2) APT revealed significant concentration profiles and partitioning of Al, Ti, and Ta into γ', while Co, Cr, Fe, Mo, W, and Re preferentially segregated into the γ matrix. Notably, the observed increase in the Re partitioning coefficient from 5.57 (Ag-1) to 7.56 (Ag-2) is a result of γ particle formation within the γ' phase, in which Re redistributes from the γ' phase into the newly formed γ particles, facilitating γ particle formation within γ' during Ag-2 treatment. This finding highlights a distinctive partitioning behavior compared to conventional superalloys, suggesting a unique kinetic pathway enabled by Re incorporation.

(3) Long-term aging experiments (750–850 °C up to 200 h) demonstrated remarkable phase stability in HESA-X1, with both γ nanoparticles and cuboidal γ' precipitates maintaining size and morphology. The coarsening rate constant (K) at 750 °C was calculated as 1.83×10^{-27} m^3/s, significantly lower than that of Re-free analogues (e.g., HESA-3), indicating suppressed diffusion and enhanced coarsening resistance due to the low diffusivity of Re.

In the present study, the findings underscore the critical role of Re in promoting microstructural refinement and stability by limiting atomic mobility, reducing coarsening kinetics, and enhancing phase integrity. The approach demonstrated here provides a framework for designing next-generation superalloys that leverage controlled partitioning behavior and diffusion kinetics to achieve superior thermal and mechanical stability.

Author Contributions: Conceptualization, W.-C.H., H.M. and A.-C.Y.; methodology, W.-C.H., H.M. and A.-C.Y.; validation, W.-C.H.; formal analysis, W.-C.H., T.S. (Takuma Saito) and M.S.; investigation, W.-C.H., T.S. (Takuma Saito) and M.S.; resources, T.S. (Taisuke Sasaki), W.-C.H., T.S. (Takuma Saito) and M.S.; writing—original draft preparation, W.-C.H.; writing—review and editing, A.-C.Y., M.S. and T.S. (Takuma Saito); visualization, W.-C.H. and T.S. (Takuma Saito); supervision, H.M., T.S. (Taisuke Sasaki) and A.-C.Y.; funding acquisition, H.M. and A.-C.Y. All authors have read and agreed to the published version of the manuscript.

Funding: This research was funded by the "High Entropy Materials Center" from The Featured Areas Research Center Program within the framework of the Higher Education Sprout Project by the Ministry of Education (MOE) in Taiwan, R.O.C. This research was also funded by the National Science and Technology Council (NSTC) in Taiwan, R.O.C. under Grant NSTC 112-2927-I-007-504, NSTC 110-2221-E-007-020-MY3, NSTC 112-2224-E-007-003, NSTC 113-2221-E-007-035. Wei-Che Hsu would like to thank the National Institute for Materials Science (NIMS) in Japan for the provision of the International Collaborative Graduate Program (ICGP) scholarship.

Data Availability Statement: The data that supports the findings of this study are available from the author upon reasonable request.

Acknowledgments: Wei-Che Hsu would like to thank Anna M. Manzoni from Department of Materials Engineering, Bundesanstalt für Materialforschung und -prüfung in Germany for her valuable suggestions on the manuscript preparation. Wei-Che Hsu also acknowledge Yuji Takata of NIMS for his technical support in producing the single-crystal bars of HESAs.

Conflicts of Interest: The authors declare no conflict of interest.

References

1. Yeh, J.-W.; Chen, S.K.; Lin, S.-J.; Gan, J.-Y.; Chin, T.-S.; Shun, T.-T.; Tsau, C.-H.; Chang, S.-Y. Nanostructured high-entropy alloys with multiple principal elements: Novel alloy design concepts and outcomes. *Adv. Eng. Mater.* **2004**, *6*, 299–303. [CrossRef]
2. Qian, X.; Han, D.; Zheng, L.; Chen, J.; Tyagi, M.; Li, Q.; Du, F.; Zheng, S.; Huang, X.; Zhang, S.; et al. High-entropy polymer produces a giant electrocaloric effect at low fields. *Nature* **2021**, *600*, 664–669. [CrossRef] [PubMed]
3. Hsu, W.-L.; Tsai, C.-W.; Yeh, A.-C.; Yeh, J.-W. Clarifying the four core effects of high-entropy materials. *Nat. Rev. Chem.* **2024**, *8*, 471–485. [CrossRef] [PubMed]
4. Raza, H.; Cheng, J.; Wang, J.; Kandasamy, S.; Zheng, G.; Chen, G. Titanium-containing high entropy oxide (Ti-HEO): A redox expediting electrocatalyst towards lithium polysulfides for high performance Li-S batteries. *Nano Res. Energy* **2024**, *3*, e9120116. [CrossRef]
5. Li, L.; Zhang, M.; Jiang, M.; Gao, L.; Ma, Z.; Cao, M. High entropy ceramics for electromagnetic functional materials. *Adv. Funct. Mater.* **2024**, *35*, 2416673. [CrossRef]
6. Tung, C.-C.; Yeh, J.-W.; Shun, T.-T.; Chen, S.-K.; Huang, Y.-S.; Chen, H.-C. On the elemental effect of AlCoCrCuFeNi high-entropy alloy system. *Mater. Lett.* **2007**, *61*, 1–5. [CrossRef]
7. He, J.Y.; Liu, W.H.; Wang, H.; Wu, Y.; Liu, X.J.; Nieh, T.G.; Lu, Z.P. Effects of Al addition on structural evolution and tensile properties of the FeCoNiCrMn high-entropy alloy system. *Acta Mater.* **2014**, *62*, 105–113. [CrossRef]
8. Hsu, C.Y.; Yeh, J.W.; Chen, S.K.; Shun, T.T. Wear resistance and high-temperature compression strength of Fcc CuCoNiCrAl0. 5Fe alloy with boron addition. *Metall. Mater. Trans. A* **2004**, *35*, 1465–1469. [CrossRef]
9. Chuang, M.-H.; Tsai, M.-H.; Wang, W.-R.; Lin, S.-J.; Yeh, J.-W. Microstructure and wear behavior of AlxCo1. 5CrFeNi1. 5Tiy high-entropy alloys. *Acta Mater.* **2011**, *59*, 6308–6317. [CrossRef]
10. Lee, C.; Chang, C.; Chen, Y.; Yeh, J.; Shih, H. Effect of the aluminium content of AlxCrFe1. 5MnNi0. 5 high-entropy alloys on the corrosion behaviour in aqueous environments. *Corros. Sci.* **2008**, *50*, 2053–2060. [CrossRef]
11. Chou, Y.; Wang, Y.; Yeh, J.; Shih, H. Pitting corrosion of the high-entropy alloy Co1. 5CrFeNi1. 5Ti0. 5Mo0. 1 in chloride-containing sulphate solutions. *Corros. Sci.* **2010**, *52*, 3481–3491. [CrossRef]

12. He, J.Y.; Wang, H.; Huang, H.L.; Xu, X.D.; Chen, M.W.; Wu, Y.; Liu, X.J.; Nieh, T.G.; An, K.; Lu, Z.P. A precipitation-hardened high-entropy alloy with outstanding tensile properties. *Acta Mater.* **2016**, *102*, 187–196. [CrossRef]
13. Tong, Y.; Chen, D.; Han, B.; Wang, J.; Feng, R.; Yang, T.; Zhao, C.; Zhao, Y.L.; Guo, W.; Shimizu, Y. Outstanding tensile properties of a precipitation-strengthened FeCoNiCrTi0. 2 high-entropy alloy at room and cryogenic temperatures. *Acta Mater.* **2019**, *165*, 228–240. [CrossRef]
14. Zhang, W.; Chabok, A.; Wang, H.; Shen, J.; Oliveira, J.P.; Feng, S.; Schell, N.; Kooi, B.J.; Pei, Y. Ultra-strong and ductile precipitation-strengthened high entropy alloy with 0.5% Nb addition produced by laser additive manufacturing. *J. Mater. Sci. Technol.* **2024**, *187*, 195–211. [CrossRef]
15. Włoczewski, M.; Jasiewicz, K.; Jenczyk, P.; Gadalińska, E.; Kulikowski, K.; Zhang, Y.; Li, R.X.; Jarząbek, D.M. AlCoCrFeNiTi0. 2 High-Entropy Alloy Under Plasma Nitriding: Complex Microstructure Transformation, Mechanical and Tribological Enhancement. *Met. Mater. Trans. A* **2025**, *56*, 2040–2056. [CrossRef]
16. Alvi, S.; Milczarek, M.; Jarzabek, D.M.; Hedman, D.; Kohan, M.G.; Levintant-Zayonts, N.; Vomiero, A.; Akhtar, F. Enhanced mechanical, thermal and electrical properties of high-entropy HfMoNbTaTiVWZr thin film metallic glass and its nitrides. *Adv. Eng. Mater.* **2022**, *24*, 2101626. [CrossRef]
17. Martin, P.; Aguilar, C.; Cabrera, J. A review on mechanical alloying and spark plasma sintering of refractory high-entropy alloys: Challenges, microstructures, and mechanical behavior. *J. Mater. Res. Technol.* **2024**, *30*, 1900–1928. [CrossRef]
18. Shen, X.; Guo, Z.; Liu, F.; Dong, F.; Zhang, Y.; Liu, C.; Wang, B.; Luo, L.; Su, Y.; Cheng, J.; et al. Microstructural evolution and mechanical behavior of novel TiZrTaxNbMo refractory high-entropy alloys. *J. Alloys Compd.* **2024**, *990*, 174459. [CrossRef]
19. Manzoni, A.M.; Glatzel, U. New multiphase compositionally complex alloys driven by the high entropy alloy approach. *Mater. Charact.* **2019**, *147*, 512–532. [CrossRef]
20. Sahragard-Monfared, G.; Belcher, C.H.; Bajpai, S.; Wirth, M.; Devaraj, A.; Apelian, D.; Lavernia, E.J.; Ritchie, R.O.; Minor, A.M.; Gibeling, J.C.; et al. Tensile creep behavior of the Nb45Ta25Ti15Hf15 refractory high entropy alloy. *Acta Mater.* **2024**, *272*, 119940. [CrossRef]
21. Sengupta, A.; Putatunda, S.K.; Bartosiewicz, L.; Hangas, J.; Nailos, P.J.; Peputapeck, M.; Alberts, F.E. Tensile behavior of a new single-crystal nickel-based superalloy (CMSX-4) at room and elevated temperatures. *J. Mater. Eng. Perform.* **1994**, *3*, 73–81. [CrossRef]
22. Reed, R.C. *The Superalloys: Fundamentals and Applications*; Cambridge University Press: Cambridge, UK, 2008.
23. Long, H.; Mao, S.; Liu, Y.; Zhang, Z.; Han, X. Microstructural and compositional design of Ni-based single crystalline superalloys—A review. *J. Alloys Compd.* **2018**, *743*, 203–220. [CrossRef]
24. Yeh, A.C.; Tsao, T.K.; Chang, Y.J.; Chang, K.C.; Yeh, J.W.; Chiou, M.S.; Jian, S.R.; Kuo, C.M.; Wang, W.R.; Murakami, H. Developing new type of high temperature alloys–high entropy superalloys. *Int. J. Metall. Mater. Eng.* **2015**, *1*, 1–4.
25. Detrois, M.; Jablonski, P.D.; Antonov, S.; Li, S.; Ren, Y.; Tin, S.; Hawk, J.A. Design and thermomechanical properties of a γ' precipitate-strengthened Ni-based superalloy with high entropy γ matrix. *J. Alloys Compd.* **2019**, *792*, 550–560. [CrossRef]
26. Chen, Y.-T.; Chang, Y.-J.; Murakami, H.; Gorsse, S.; Yeh, A.-C. Designing high entropy superalloys for elevated temperature application. *Scr. Mater.* **2020**, *187*, 177–182. [CrossRef]
27. Tsao, T.; Yeh, A.; Kuo, C.; Murakami, H. On The Superior High Temperature Hardness of Precipitation Strengthened High Entropy Ni-Based Alloys. *Adv. Eng. Mater.* **2016**, *19*, 1600475. [CrossRef]
28. Tsao, T.-K.; Yeh, A.-C.; Kuo, C.-M.; Kakehi, K.; Murakami, H.; Yeh, J.-W.; Jian, S.-R. The high temperature tensile and creep behaviors of high entropy superalloy. *Sci. Rep.* **2017**, *7*, 12658. [CrossRef] [PubMed]
29. Chen, Y.-T.; Chang, Y.-J.; Murakami, H.; Sasaki, T.; Hono, K.; Li, C.-W.; Kakehi, K.; Yeh, J.-W.; Yeh, A.-C. Hierarchical microstructure strengthening in a single crystal high entropy superalloy. *Sci. Rep.* **2020**, *10*, 12163. [CrossRef] [PubMed]
30. Antonov, S.; Detrois, M.; Isheim, D.; Seidman, D.; Helmink, R.C.; Goetz, R.L.; Sun, E.; Tin, S. Comparison of thermodynamic database models and APT data for strength modeling in high Nb content γ–γ' Ni-base superalloys. *Mater. Des.* **2015**, *86*, 649–655. [CrossRef]
31. Sulzer, S.; Hasselqvist, M.; Murakami, H.; Bagot, P.; Moody, M.; Reed, R. The effects of chemistry variations in new nickel-based superalloys for industrial gas turbine applications. *Met. Mater. Trans. A* **2020**, *51*, 4902–4921. [CrossRef]
32. Giraud, R.; Cormier, J.; Hervier, Z.; Bertheau, D.; Harris, K.; Wahl, J.; Milhet, X.; Mendez, J.; Organista, A. Effect of the prior microstructure degradation on the high temperature/low stress non-isothermal creep behavior of cmsx-4® Ni-based single crystal superalloy. *Superalloys* **2012**, *2012*, 265–274.
33. Cormier, J. Thermal cycling creep resistance of Ni-based single crystal superalloys. *Superalloys* **2016**, *2016*, 385–394.
34. Lifshitz, I.; Slyozov, V. The kinetics of precipitation from supersaturated solid solutions. *J. Phys. Chem. Solids* **1961**, *19*, 35–50. [CrossRef]
35. Wagner, C. Theorie der alterung von niederschlägen durch umlösen (Ostwald-reifung). *Z. Elektrochem. Berichte Bunsenges. Phys. Chem.* **1961**, *65*, 581–591. [CrossRef]

36. Wang, Y.; Tang, J.; Fujihara, H.; Adachi, N.; Todaka, Y.; Xu, Y.; Saha, M.; Sasaki, T.; Shimizu, K.; Hirayama, K.; et al. Advancing the hydrogen tolerance of ultrastrong aluminum alloys via nanoprecipitate modification. *Corros. Sci.* **2024**, *240*, 112471. [CrossRef]
37. Wang, B.; Zhang, J.; Huang, T.; Su, H.; Li, Z.; Liu, L.; Fu, H. Influence of W, Re, Cr, and Mo on microstructural stability of the third generation Ni-based single crystal superalloys. *J. Mater. Res.* **2016**, *31*, 3381–3389. [CrossRef]
38. Uddagiri, M.; Shchyglo, O.; Steinbach, I.; Tegeler, M. Solidification of the Ni-based superalloy CMSX-4 simulated with full complexity in 3-dimensions. *Prog. Addit. Manuf.* **2024**, *9*, 1185–1196. [CrossRef]
39. Jablonski, P.D.; Cowen, C.J. Homogenizing a nickel-based superalloy: Thermodynamic and kinetic simulation and experimental results. *Met. Mater. Trans. B* **2009**, *40*, 182–186. [CrossRef]
40. Xinxu, L.; Chonglin, J.; Yong, Z.; Shaomin, L.; Zhouhua, J. Segregation and homogenization for a new nickel-based superalloy. *Vacuum* **2020**, *177*, 109379. [CrossRef]
41. Okugawa, M.; Izumikawa, D.; Koizumi, Y. Simulations of non-equilibrium and equilibrium segregation in nickel-based superalloy using modified Scheil-Gulliver and phase-field methods. *Mater. Trans.* **2020**, *61*, 2072–2078. [CrossRef]
42. Paraschiv, A.; Matache, G.; Puscasu, C. The effect of heat treatment on the homogenization of CMSX-4 Single-Crystal Ni-Based Superalloy. *Transp. Res. Procedia* **2018**, *29*, 303–311. [CrossRef]
43. Tai, W.; Zhang, R.; Cui, C.; Zhou, Z.; Zhou, Y.; Sun, X. Solidification segregation behavior and homogenization process of a difficult-to-deform superalloy used at 850° C. *Crystals* **2023**, *13*, 1582. [CrossRef]
44. Matache, G.; Stefanescu, D.M.; Puscasu, C.; Alexandrescu, E. An Investigation of dendritic segregation in directionally solidified CMSX-4 superalloy. In *Advances in the Science and Engineering of Casting Solidification: An MPMD Symposium Honoring Doru Michael Stefanescu*; Springer: Cham, Switzerland, 2016; pp. 223–230.
45. Xu, Q.; Zhang, Y. Precipitation and growth simulation of γ' phase in single crystal superalloy DD6 with multiphase-field method and explicit nucleation algorithm. *Metals* **2020**, *10*, 1346. [CrossRef]
46. Schleifer, F.; Fleck, M.; Holzinger, M.; Lin, Y.-Y.; Glatzel, U. Phase-field modeling of γ' and γ'' precipitate size evolution during heat treatment of Ni-based superalloys. In Proceedings of the Superalloys 2020: Proceedings of the 14th International Symposium on Superalloys, Seven Springs, PA, USA, 13–17 September 2020; Springer: Cham, Switzerland, 2020; pp. 500–508.
47. Nathal, M.V.; MacKay, R.A.; Miner, R.V. Influence of precipitate morphology on intermediate temperature creep properties of a nickel-base superalloy single crystal. *Met. Trans. A* **1989**, *20*, 133–141. [CrossRef]
48. Murakumo, T.; Kobayashi, T.; Koizumi, Y.; Harada, H. Creep behaviour of Ni-base single-crystal superalloys with various γ' volume fraction. *Acta Mater.* **2004**, *52*, 3737–3744. [CrossRef]
49. Saito, T.; Ishida, A.; Yuyama, M.; Takata, Y.; Kawagishi, K.; Yeh, A.-C.; Murakami, H. Tensile creep behavior of single-crystal high-entropy superalloy at intermediate temperature. *Crystals* **2020**, *11*, 28. [CrossRef]
50. Sugui, T.; Minggang, W.; Tang, L.; Benjiang, Q.; Jun, X. Influence of TCP phase and its morphology on creep properties of single crystal nickel-based superalloys. *Mater. Sci. Eng. A* **2010**, *527*, 5444–5451. [CrossRef]
51. Rakoczy, Ł.; Grudzień-Rakoczy, M.; Cygan, R.; Kargul, T.; Maj, Ł.; Zielińska-Lipiec, A. Analysis of the as-cast microstructure and properties of the Ni-based superalloy MAR-M247® produced via directional solidification. *Met. Mater. Trans. A* **2023**, *54*, 3630–3652. [CrossRef]
52. Zhao, Y.; Xiong, W. Influence of Homogenization on Phase Transformations during Isothermal Aging of Inconel 718 Superalloys Fabricated by Additive Manufacturing and Suction Casting. *Materials* **2023**, *16*, 4968. [CrossRef] [PubMed]
53. Meher, S.; Aagesen, L.K.; Carroll, M.C.; Pollock, T.M.; Carroll, L.J. The origin and stability of nanostructural hierarchy in crystalline solids. *Sci. Adv.* **2018**, *4*, eaao6051. [CrossRef] [PubMed]
54. Smith, T.; Rao, Y.; Wang, Y.; Ghazisaeidi, M.; Mills, M. Diffusion processes during creep at intermediate temperatures in a Ni-based superalloy. *Acta Mater.* **2017**, *141*, 261–272. [CrossRef]
55. Gorsse, S.; Chen, Y.-T.; Hsu, W.-C.; Murakami, H.; Yeh, A.-C. Modeling the precipitation processes and the formation of hierarchical microstructures in a single crystal high entropy superalloy. *Scr. Mater.* **2021**, *193*, 147–152. [CrossRef]
56. Giamei, A.F.; Anton, D.L. Rhenium additions to a Ni-base superalloy: Effects on microstructure. *Met. Trans. A* **1985**, *16*, 1997–2005. [CrossRef]
57. Fährmann, M.; Wolf, J.; Pollock, T. The influence of microstructure on the measurement of γ-γ' lattice mismatch in single-crystal Ni-base superalloys. *Mater. Sci. Eng. A* **1996**, *210*, 8–15. [CrossRef]
58. Harada, H.; Murakami, H. Design of Ni-base superalloys. In *Computational Materials Design*; Springer: Berlin/Heidelberg, Germany, 1999; pp. 39–70.
59. Giese, S.; Bezold, A.; Pröbstle, M.; Heckl, A.; Neumeier, S.; Göken, M. The importance of diffusivity and partitioning behavior of solid solution strengthening elements for the high temperature creep strength of Ni-base superalloys. *Met. Mater. Trans. A* **2020**, *51*, 6195–6206. [CrossRef]
60. Zhang, J.; Huang, T.; Lu, F.; Cao, K.; Wang, D.; Zhang, J.; Zhang, J.; Su, H.; Liu, L. The effect of rhenium on the microstructure stability and γ/γ' interfacial characteristics of Ni-based single crystal superalloys during long-term aging. *J. Alloys Compd.* **2021**, *876*, 160114. [CrossRef]

61. Durst, K.; Göken, M. Micromechanical characterisation of the influence of rhenium on the mechanical properties in nickel-base superalloys. *Mater. Sci. Eng. A* **2004**, *387-389*, 312–316. [CrossRef]
62. Neumeier, S.; Pyczak, F.; Göken, M. The influence of Ruthenium and Rhenium on the local properties of the γ-and γ′-phase in Nickel-base superalloys and their consequences for alloy behavior. *Superalloys* **2008**, *2008*, 109–119.
63. Caron, P.; Khan, T. Evolution of Ni-based superalloys for single crystal gas turbine blade applications. *Aerosp. Sci. Technol.* **1999**, *3*, 513–523. [CrossRef]
64. Caron, P.; Khan, T. Improvement of creep strength in a nickel-base single-crystal superalloy by heat treatment. *Mater. Sci. Eng.* **1983**, *61*, 173–184. [CrossRef]
65. Nathal, M.V. Effect of initial gamma prime size on the elevated temperature creep properties of single crystal nickel base superalloys. *Met. Trans. A* **1987**, *18*, 1961–1970. [CrossRef]
66. Xia, P.; Yu, J.; Sun, X.; Guan, H.; Hu, Z. Influence of γ′ precipitate morphology on the creep property of a directionally solidified nickel-base superalloy. *Mater. Sci. Eng. A* **2008**, *476*, 39–45. [CrossRef]
67. Huang, Y.; Wang, X.; Cui, C.; Li, J.; Ye, L.; Hou, G.; Yang, Y.; Liu, J.; Liu, J.; Zhou, Y.; et al. The effect of coarsening of γ′ precipitate on creep properties of Ni-based single crystal superalloys during long-term aging. *Mater. Sci. Eng. A* **2020**, *773*, 138886. [CrossRef]
68. Baldan, A. Review progress in Ostwald ripening theories and their applications to nickel-base superalloys Part I: Ostwald ripening theories. *J. Mater. Sci.* **2002**, *37*, 2171–2202. [CrossRef]
69. Baldan, A. Review Progress in Ostwald ripening theories and their applications to the γ′-precipitates in nickel-base superalloys Part II Nickel-base superalloys. *J. Mater. Sci.* **2002**, *37*, 2379–2405. [CrossRef]
70. Yoon, K.E.; Noebe, R.D.; Seidman, D.N. Effects of rhenium addition on the temporal evolution of the nanostructure and chemistry of a model Ni–Cr–Al superalloy. I: Experimental observations. *Acta Mater.* **2007**, *55*, 1145–1157. [CrossRef]
71. Tiley, J.; Viswanathan, G.; Srinivasan, R.; Banerjee, R.; Dimiduk, D.; Fraser, H. Coarsening kinetics of γ′ precipitates in the commercial nickel base Superalloy René 88 DT. *Acta Mater.* **2009**, *57*, 2538–2549. [CrossRef]
72. Karunaratne, M.; Carter, P.; Reed, R. Interdiffusion in the face-centred cubic phase of the Ni–Re, Ni–Ta and Ni–W systems between 900 and 1300 C. *Mater. Sci. Eng. A* **2000**, *281*, 229–233. [CrossRef]
73. Campbell, C.; Boettinger, W.; Kattner, U. Development of a diffusion mobility database for Ni-base superalloys. *Acta Mater.* **2002**, *50*, 775–792. [CrossRef]
74. Ardell, A.J.; Ozolins, V. Trans-interface diffusion-controlled coarsening. *Nat. Mater.* **2005**, *4*, 309–316. [CrossRef] [PubMed]
75. Ardell, A.J. Trans-interface-diffusion-controlled coarsening of γ′ precipitates in ternary Ni–Al–Cr alloys. *Acta Mater.* **2013**, *61*, 7828–7840. [CrossRef]
76. Ardell, A.J. Quantitative predictions of the trans-interface diffusion-controlled theory of particle coarsening. *Acta Mater.* **2010**, *58*, 4325–4331. [CrossRef]
77. Pandey, P.; Sawant, A.; Nithin, B.; Peng, Z.; Makineni, S.; Gault, B.; Chattopadhyay, K. On the effect of Re addition on microstructural evolution of a CoNi-based superalloy. *Acta Mater.* **2019**, *168*, 37–51. [CrossRef]